



Identification of linear response functions from arbitrary perturbation experiments in the presence of noise – Part II. Application to the land carbon cycle in the MPI Earth System Model

Guilherme L. Torres Mendonça^{1,2}, Julia Pongratz^{2,3}, and Christian H. Reick²

¹International Max Planck Research School on Earth System Modelling, Hamburg, Germany

²Max Planck Institute for Meteorology, Hamburg, Germany

³Ludwig-Maxmillians-Universität München, Munich, Germany

Correspondence: Guilherme L. Torres Mendonça (guilherme.mendonca@mpimet.mpg.de)

Abstract. The Response Function Identification method introduced in the first part of this study is applied here to investigate the land carbon cycle in the Max Planck Institute for Meteorology Earth System Model. We identify from standard C⁴MIP 1% experiments the linear response functions that generalize the land carbon sensitivities β and γ . The identification of these generalized sensitivities is shown to be robust by demonstrating their predictive power when applied to experiments not used for their identification. The linear regime for which the generalized framework is valid is estimated, and approaches to improve the quality of the results are proposed. For the generalized γ -sensitivity, the response is found to be linear for temperature perturbations until at least 6 K. When this sensitivity is identified from a $2\times\text{CO}_2$ experiment instead of the 1% experiment, its predictive power improves, indicating an enhancement in the quality of the identification. For the generalized β -sensitivity, the linear regime is found to extend up to CO_2 perturbations of 100 ppm. We find that nonlinearities in the β -response arise mainly from the nonlinear relationship between Net Primary Production and CO_2 . By taking instead of CO_2 the resulting Net Primary Production as forcing, the response is approximately linear until CO_2 perturbations of about 850 ppm. Taking Net Primary Production as forcing also substantially improves the spectral resolution of the generalized β -sensitivity. For the best recovery of this sensitivity, we find a spectrum of internal time scales with two peaks, at 4 and 100 years. Robustness of this result is demonstrated by two independent tests. We find that the two-peak spectrum can be explained by the different characteristic time scales of functionally different elements of the land carbon cycle. The peak at 4 years results from the collective response of carbon pools whose dynamics is governed by fast processes, namely pools representing living vegetation tissues (leaves, fine roots, sugars, and starches) and associated litter. The peak at 100 years results from the collective response of pools whose dynamics is determined by slow processes, namely the pools that represent the wood in stem and coarse roots, the associated litter, and the soil carbon (humus). Analysis of the response functions that characterize these two groups of pools shows that the pools with fast dynamics dominate the land carbon response only for times below 2 years. For times above 25 years the response is completely determined by the pools with slow dynamics. From 100 years onwards only the humus pool contributes to the land carbon response.



1 Introduction

In Part I of this study we developed a method to identify linear response functions from arbitrary perturbation experiments. The RFI method (Response Function Identification method) was tested by means of artificial toy model simulations. Here, we demonstrate the applicability of our method to a practical problem: We investigate the dynamics of the land carbon cycle in the Max Planck Institute for Meteorology Earth System Model (MPI-ESM; see Appendix A). In particular, we show how our RFI method provides insight into two aspects of central relevance to carbon-cycle research: The sensitivity of the land carbon cycle to changes in atmospheric CO₂ and its distribution of internal time scales.

The global carbon cycle plays a critical role in mitigating climatic effects from CO₂ emissions. According to the yearly published Global Carbon Budget (Friedlingstein et al., 2020), about half of the anthropogenic CO₂ emitted from pre-industrial times to 2019 has been taken up from the atmosphere by the ocean and the terrestrial biosphere. Despite its relevance to climate, the dynamics of the carbon cycle is still poorly understood (Ilyina and Friedlingstein, 2016). Improving our understanding of this dynamics, in particular in response to CO₂ perturbations, is therefore one of the major challenges of climate research (Marotzke et al., 2017).

The most advanced tools used to study the response of the carbon cycle to perturbations and its effect on climate are known as Earth System Models, which are complex numerical models that simulate the interaction between climate and the carbon cycle. To systematically investigate this interaction, for more than a decade now internationally coordinated simulation exercises have been performed with several Earth System Models within the Coupled Climate Carbon Cycle Model Intercomparison Project (C⁴MIP; see Fung et al., 2000; Friedlingstein et al., 2006) that today belongs to the international Coupled Model Intercomparison Project (CMIP; see Taylor et al., 2012). Results from such exercises show a general agreement across models in the ocean carbon response, while the response of land carbon presents a large model spread (Friedlingstein et al., 2006; Arora et al., 2013, 2019).

To better understand the reasons for this spread one may follow a top-down strategy by investigating which processes dominate the various contributions to the global response. A typical approach in this direction is to consider two global-scale contributions: One arising from the sensitivity of the land carbon cycle to the radiative effect of CO₂ acting via greenhouse warming, and another from its sensitivity to the biochemical effect of CO₂ concentrations on photosynthetic carbon assimilation (Arora et al., 2013; Schwinger et al., 2014; Adloff et al., 2018; Arora et al., 2019). The magnitude of each of these sensitivities is quantified by the γ and β values introduced by Friedlingstein et al. (2003). But although these values give insight into the magnitude of the sensitivities, they cannot be seen as properties of the land carbon cycle alone. The reason is that γ and β quantify the sensitivity of land carbon to CO₂ perturbations only for a particular perturbation scenario, so that for different scenarios one may obtain different values (Gregory et al., 2009; Arora et al., 2013).

To quantify this sensitivity in a more systematic way and thereby gain deeper insight into the land carbon dynamics one needs a more general formalism. For small changes in atmospheric CO₂ one can show that by accounting for the memory of the carbon cycle these values are generalized to linear response functions, which in turn can be seen as properties of the land carbon cycle itself (Rubino et al., 2016; Enting and Clisby, 2019, see also Appendix B). As a result, these linear response



functions characterize the land carbon sensitivities for any perturbation scenario. For this reason these functions will here be called land carbon *generalized sensitivities*.

The essential step to investigate the carbon-cycle dynamics within this general formalism is the identification of the generalized sensitivities. Typically, the γ and β values proposed by Friedlingstein et al. (2003) are obtained taking data from standardized C⁴MIP simulation experiments where, starting from an equilibrium state, atmospheric CO₂ concentration is increased by 1% each year. Since data from such 1% experiments performed with several Earth System Models are readily available in international databases, one would be interested in identifying the generalized γ - and β -sensitivities as well from these experiments. But methods in the literature to identify response functions from data require special perturbation experiments, and C⁴MIP experiments were not tailored for this purpose. It is here that our RFI method is useful: Because it was designed to derive response functions from experiments driven by any arbitrary perturbation, in the present study we show that by this method one can robustly derive the land carbon generalized sensitivities for the MPI-ESM taking data from standard C⁴MIP 1% experiments. To make sure the identified generalized sensitivities are indeed characteristics of the land carbon cycle in the MPI-ESM, we demonstrate their predictive power by applying them to predict the response of the model in several experiments that were not used for their identification. In preparation for future studies applying these generalized sensitivities to study the dynamics of the carbon-climate system in C⁴MIP models, we also investigate various ideas to improve the quality of the recovery of the response functions by using additional types of data routinely available in C⁴MIP simulations or using log-transformed data to account at least partially for process-immanent nonlinearities that hinder the usage of experiment data from larger levels of forcing.

Apart from giving a systematic quantification of the sensitivities, linear response functions can be a powerful tool to gain insight into the internal dynamics of the carbon cycle. Because response functions fully characterize the linear response of a system, they contain information on its distribution of internal time scales, i.e. the weights with which characteristic time scales from internal processes contribute to the macroscopic response of the system. These weights may shed light into which are the most relevant processes to the response at different time scales. For our application to the land carbon, such information may give hints into the main processes influencing the model spread found in the C⁴MIP results.

But while several studies have tried to obtain the weights of different time scales in the carbon cycle by fitting response functions to a sum of few exponents (Maier-Reimer and Hasselmann, 1987; Enting and Mansbridge, 1987; Enting, 1990; Joos et al., 1996; Pongratz et al., 2011; Joos et al., 2013; Colbourn et al., 2015; Lord et al., 2016), in principle it is not clear to what extent such results can be trusted, let alone interpreted. The reason is that finding these weights from data is a severely ill-posed problem that requires special methods to be dealt with (Istratov and Vyvenko, 1999). In contrast to the classical fitting procedures, by employing a regularization technique (Groetsch, 1984; Engl et al., 1996) combined with a novel estimation of the noise level in the data (see Part I) our RFI method accounts for this ill-posedness. In addition, instead of assuming that the response functions result from only few time scales, the RFI method recovers a continuous spectrum of time scales, in agreement with what one would expect when studying the carbon cycle response (Forney and Rothman, 2012a). In the present work we show that, in contrast to results obtained with classical fitting procedures, spectra recovered by the RFI method may be *reliable* and even *interpretable*. For this purpose, we investigate a relatively detailed spectrum of time scales that arises from



a high-quality recovery of the generalized β -sensitivity. We examine (i) the robustness of the obtained spectrum and (ii) the explanation for its time-scale structure.

An additional novelty introduced here is a simple procedure to estimate the linear regime of the response, i.e. the range of
95 perturbation strengths for which the response of the system can be considered linear. As discussed in Part I, the presence of
traces of nonlinear responses in the data can severely deteriorate the recovery of the response function. Hence, to make sure
that the data from which the response function is recovered contain no strong nonlinearities, one must be able to estimate the
linear regime of the response. Because the response functions will be derived from 1% experiments, we introduce a technique
to estimate with the aid of additional simulations the linear regime from this type of experiment. By this technique the linear
100 regime of the response of land carbon to changes in CO₂ and climate for the MPI-ESM will be estimated.

The outline of the paper is as follows. In the next section we introduce the methodology of the study including the RFI
method, the C⁴MIP experiments, and the technique to estimate the linear regime of the response from “percent” experiments.
In sections 3 and 4 we identify and investigate the generalization of the γ - and β -sensitivities in the MPI-ESM. In section
5 we investigate the detailed spectrum of time scales obtained for the generalized β -sensitivity. In section 6 the results are
105 summarized and discussed.

2 Methodology

In this section we introduce the methodology employed throughout the study. We start by briefly introducing the RFI method
(for a detailed description please refer to Part I), the C⁴MIP-type experiments considered here, and technical details for the
identification of the generalized sensitivities. Then, we present our procedure to estimate the linear regime of the response from
110 “percent” experiments.

2.1 RFI method and C⁴MIP experiments

The RFI method identifies the response function $\chi(t)$ taking data from the response $Y(t)$ – in our example the global land
carbon – and the perturbation $f(t)$ – atmospheric CO₂ or temperature (see below) – assuming the following ansatz based on
linear response theory (see Part I):

$$115 \quad \Delta Y(t) = \int_0^t \chi(t-s) \Delta f(s) ds + \eta(t), \quad (1)$$

where $\eta(t)$ is a noise term. Here $\Delta Y(t)$ and $\Delta f(t)$ mean that we are taking only the change in the variables with respect
to their equilibrium values from a control simulation. Following Forney and Rothman (2012a), the spectrum of internal time
scales is obtained by assuming that the response function $\chi(t)$ can be represented by an overlay of exponential modes:

$$\chi(t) = \int_0^\infty g(\tau) e^{-t/\tau} d\tau. \quad (2)$$



120 To account for the large range of time scales in the carbon cycle (Ciais et al., 2013) it is useful to rewrite Eq. (2) in terms of $\log_{10} \tau$, so that

$$\chi(t) = \int_{-\infty}^{\infty} q(\tau) e^{-t/\tau} d\log_{10} \tau, \quad \text{with} \quad q(\tau) := \tau \ln(10) g(\tau). \quad (3)$$

The spectrum of time scales is then given by $q(\tau)$, which following the terminology from Part I we call simply *spectrum*. The problem is solved by discretizing Eq. (1) and Eq. (3), prescribing a distribution of time scales τ , taking the data on $\Delta Y(t)$ and $\Delta f(t)$, and solving a minimization procedure for the spectrum $q(\tau)$. The parameters to prescribe the distribution of time scales are taken identically to those chosen for the application to the toy model in Part I. To treat the ill-posedness we employ Tikhonov-Phillips regularization (Phillips, 1962; Tikhonov, 1963) in a Singular Value Decomposition (SVD) framework that gives the solution by the expansion (Hansen, 2010; Bertero, 1989)

$$\mathbf{q}_\lambda = \sum_{i=0}^{M-1} f_i(\lambda) \frac{\mathbf{u}_i \bullet \Delta \mathbf{Y}}{\sigma_i} \mathbf{v}_i, \quad (4)$$

130 where M is the number of time scales, \mathbf{u}_i and \mathbf{v}_i are the singular vectors, σ_i are the singular values, λ is the regularization parameter, and $f_i(\lambda)$ are the filter functions

$$f_i(\lambda) = \frac{\sigma_i^2}{\sigma_i^2 + \lambda}. \quad (5)$$

The regularization parameter λ is determined by the discrepancy method (Morozov, 1966) with noise level estimated from a SVD analysis of the data combined with information from the control simulation. Once the spectrum \mathbf{q}_λ is found, the response function $\chi(t)$ follows from Eq. (3).

All linear response functions are identified by the RFI method taking data from C⁴MIP-type experiments performed with the MPI-ESM. We focus on identifying the response functions from standard 1% experiments that are widely available in international databases. In addition, to examine the quality of the results, we identify as well some response functions taking data from additional experiments. To investigate the robustness of the identified response functions, we employ them to predict the response of the MPI-ESM in several experiments not used for the identification. A summary of the experiments considered in the study is given in Table 1, with forcing scenarios shown in Fig. 1.

The variables taken for the identification of the response functions are the ones relevant for the quantification of the land carbon sensitivities γ and β , respectively:

- (a) The change in global land carbon in response to changes in global land temperature;
- 145 (b) The change in global land carbon in response to changes in atmospheric CO₂.

Global land carbon is computed as the sum of the total land carbon over all grid cells of the model. Global land temperature is calculated as the mean near-surface air temperature over land at 2 m height. The changes are computed as $\Delta Y(t) = Y(t) - Y_{PI}$, with Y_{PI} being the mean value of observable Y from a control simulation at pre-industrial conditions. Since the main interest lies in long-term variations, annual mean data are used.



150 As demonstrated in Appendix C, the generalization of the β -sensitivity can be shown to be monotonic. Therefore, in the following we will derive it employing the additional noise level adjustment in the RFI algorithm (step 6 of Fig. 1 in Part I). Since the generalization of the γ -sensitivity is not known to be monotonic, for this sensitivity the RFI algorithm will be applied without the additional adjustment.

Table 1. C⁴MIP-type experiments considered in this study. Forcings are shown in Fig. 1. Acronyms “rad” and “bgc” refer to standard CMIP model setups used to calculate the climate-carbon cycle sensitivities. In the “rad” (radiatively coupled) setup only the radiation code of the model is affected by changes in atmospheric CO₂. This setup is used to calculate γ . In the “bgc” (biogeochemically coupled) setup only the biogeochemistry of the model is affected by changes in atmospheric CO₂. This setup is used to calculate β . In brackets are names of standard CMIP experiments.

Type	Forcing	Description
Percent	0.5% rad	CO ₂ is increased from its pre-industrial value at the specified percent rate per year.
	0.5% bgc	
	0.75% rad	
	0.75% bgc	
	1% rad (esmFdbk1)	
	1% bgc (esmFixClim1)	
	1.5% rad	
	1.5% bgc	
	2% rad	
	2% bgc	
Step	1.1 × CO ₂ rad	CO ₂ is abruptly increased from its pre-industrial value by the specified factor.
	1.1 × CO ₂ bgc	
	2 × CO ₂ rad	
	2 × CO ₂ bgc	
Control	pre-industrial (piControl)	CO ₂ is held fixed at its pre-industrial value.

155 2.2 Estimating the linear regime from “percent” experiments

As described in Part I, the recovery of response functions is cursed by the presence of noise and nonlinearities. The RFI method is designed to cope with the former. In the present section we present a technique to cope with the latter, but at the expense of performing additional response experiments. This technique will serve as a complement to the RFI method in the application to the land carbon cycle in the following sections. By these additional experiments we will determine the range of forcing

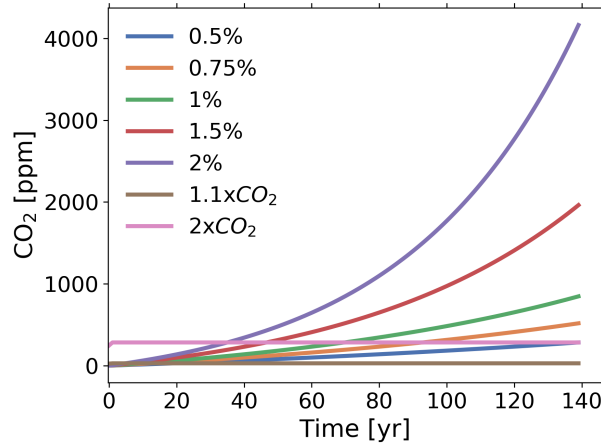


Figure 1. Forcings for the C⁴MIP-type experiments considered in this study.

160 strengths for which the response can be considered linear – an analysis in general not possible using only the control and
 perturbation experiments on which the RFI method is based.

To introduce this technique we use the example of simulations with the linear toy model employed in Part I. To demonstrate
 the effect of nonlinearities on the recovery of $\chi(t)$, following Part I we artificially add a nonlinear term $-aY^2(t)$ to the linear
 response $Y(t)$ of the toy model:

165 $Y_{nonlin}(t) := Y(t) - aY^2(t).$ (6)

In this way we obtain a nonlinear response $Y_{nonlin}(t)$, with nonlinearity strength controlled by the parameter a , from which
 $\chi(t)$ is derived. In addition to including this nonlinear term in the toy model response, to introduce the technique we will need
 to quantify the quality of the recovery of the response function. Since in our application to the land carbon the “true” response
 function is not known a priori, following Part I we quantify the quality of the recovery indirectly by measuring the quality with
 170 which the recovered response function can predict the response of the model in experiments not used for the recovery itself.
 For this purpose we introduce the *prediction error*

$$\varepsilon_k := \frac{\|\Delta Y^k - \chi \star \Delta f^k\|}{\|\Delta Y^k\|}, \quad (7)$$

where \star stands for the convolution operation, ΔY^k and Δf^k are the response and the perturbation in experiment “k”, and χ
 is the response function recovered from the 1% experiment.

175 We can now present our technique. Taking first a purely linear situation ($a = 0$) we show in Fig. 2(a) the prediction error (7)
 when using the response function obtained from a 1% simulation to predict the response from two other %-simulations with
 smaller growth rate. More precisely, performing a sequence of 1% experiments for increasingly longer simulation periods, we
 calculated for each experiment the response function and used it to predict the response for a 0.5% and 0.75% experiment

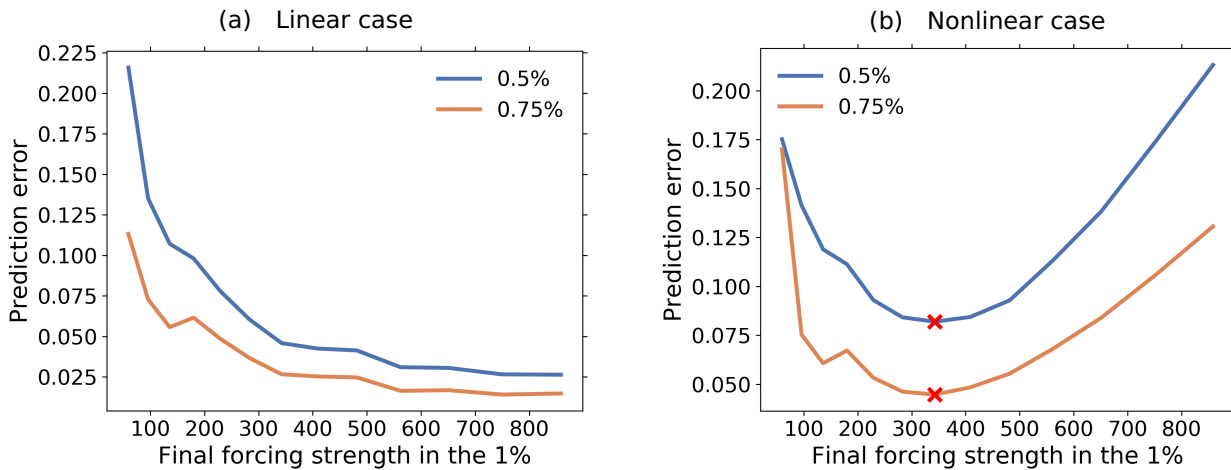


Figure 2. Toy model example for the identification of the linear regime by using additional experiments. Shown is the prediction error (7) for the response of 0.5% and 0.75% experiments as obtained from the response function calculated by the RFI method from 1% experiments. The prediction errors are plotted against the final forcing strengths of a sequence of 1% experiments with increasing time series length. The crosses at the minima indicate the final forcing strength for which the response function is optimally recovered (see text). Subfigure (a) shows the behaviour for the fully linear toy model ($a = 0$) and subfigure (b) the behaviour in the presence of nonlinear contributions to the response ($a = 5 \times 10^{-5}$). For the purpose of demonstrating more clearly the increase in the prediction error for a decrease in the forcing strength, we include in the plot cases where the forcing strength is extremely small, corresponding to very small time series lengths. To deal with such cases, we set for a number of data points $N < 30$ the number of time scales $M = N$ (see parameters for the RFI method in Part I). For such small number of time scales, usually no plateau in the singular values spectrum is found (step 2 of Fig. 1 in Part I). Therefore, for these special cases we also modify the algorithm to interpret the two smallest singular values as a plateau, since their small magnitude makes them have a similar effect to those singular values belonging to the plateau itself. In addition, to illustrate the most general case where $\chi(t)$ is not known to be monotonic, we exclude here the monotonicity check (step 6 of Fig. 1 in Part I).

180 covering the same simulation period. Then we plotted in Fig. 2(a) the prediction error against the final forcing strength of the 1% experiment. As a result, it is seen that with increasing final forcing strength the prediction error decreases. This happens because in this linear case the SNR is increasing with increasing simulation period, i.e. with increasing final forcing strength, so that the recovery of the response function continuously improves.

185 Calculating the prediction error only for experiments with smaller growth rate gets important in the next case where nonlinearities are considered (Fig. 2(b)). This plot was obtained by the same procedure except that we took for the nonlinearity parameter a value $a > 0$. As seen, in this nonlinear case the prediction error is first improving but deteriorating afterwards. For small forcing, nonlinearities are small and therefore the prediction error behaves as in the linear case, i.e. it decreases with final forcing strength. But when forcing strengths get larger, nonlinearities start to contribute substantially to the response, thereby causing a deterioration of the recovery of the response function and consequently the prediction error once more increases. This increase of the prediction error can be unambiguously traced back to the presence of nonlinearities in the 1% simulation



190 because the prediction error was calculated only for experiments with smaller growth rate, i.e. smaller forcing strength throughout the whole simulation. Therefore, nonlinearities contribute already substantially to the response in the 1% simulation before they get relevant in the other experiments. Accordingly, with this type of experiment setup we can be sure that the increase in the prediction error comes solely from the deterioration of the recovery of the response function and not from nonlinearities in the additional experiments used for calculating the prediction error.

195 Obviously, for forcing strengths smaller than at the minimum, nonlinearities do not hinder the recovery of the response function so that one can consider this to be the regime of linear system behaviour. In view of the trade-off between noise and nonlinearities, for the 1% experiment the response function is thus optimally recovered when taking as final forcing strength the value at the minimum of the prediction error curve. Similarly, if the error curve has no minimum (as in the linear case shown in Fig. 2(a)) the optimal recovery is obtained from the experiment with the largest forcing strength.

200 With the presentation of this additional technique to identify the linear regime we are ready for the application to the MPI-ESM in the next sections.

3 Generalized sensitivity χ_γ

In this section we identify from MPI-ESM simulations the linear response function χ_γ (generalization of the γ -sensitivity), defined by

$$205 \quad \Delta C^{rad}(t) = \int_0^t \chi_\gamma(t-s) \Delta T(s) ds + \eta(t), \quad (8)$$

where now the response is $\Delta Y(t) := \Delta C^{rad}(t)$ and the forcing is $\Delta f(t) := \Delta T(t)$, with $\Delta C^{rad}(t)$ being the change in global land carbon obtained in the “rad” experiment (see Table 1) and $\Delta T(t)$ the change in global land temperature.

That χ_γ indeed generalizes γ can be understood by considering that γ is defined by

$$\gamma(t) = \frac{\Delta C^{rad}(t)}{\Delta T(t)} \stackrel{(8)}{=} \frac{1}{\Delta T(t)} \int_0^t \chi_\gamma(t-s) \Delta T(s) ds, \quad (9)$$

210 for a negligible noise $\eta(t)$. From Eq. (9) it is clear that by knowing $\chi_\gamma(t)$ one can compute the response $\Delta C^{rad}(t)$ and thereby $\gamma(t)$ for any time-dependent perturbation $\Delta T(t)$, as long as the perturbation strength is small. Hence, $\chi_\gamma(t)$ can be seen as a property of the land carbon system and a generalization of $\gamma(t)$.

Estimating the linear regime

As a first step in obtaining a proper approximation of $\chi_\gamma(t)$, we investigate what maximum forcing strength can be used to assure that the recovered $\chi_\gamma(t)$ is not spoiled by the presence of nonlinearities. Using the technique introduced in section 2.2, we show in Fig. 3 the prediction error (7) for $\chi_\gamma(t)$ recovered from the 1% rad experiment as a function of the final forcing strength in the 1% rad experiment. There is no clear minimum so that for the data available the recovery of $\chi_\gamma(t)$ seems not to be limited by nonlinearities. For optimal recovery we thus take the full time series, i.e. the maximum final forcing strength.

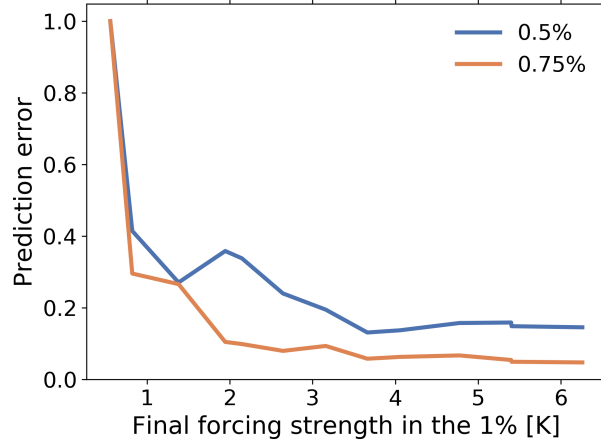


Figure 3. Prediction error (7) for the 0.5% and 0.75% rad experiments using $\chi_\gamma(t)$ recovered from the 1% rad experiment. The error is shown as function of the final forcing strength used for the recovery of $\chi_\gamma(t)$. No clear minimum is found so that the recovery seems not to be limited by nonlinearities.

χ_γ and the quality of its recovery

220 The quality of the recovery can in principle be improved by taking an experiment with better SNR. To investigate if the recovery from the 1% rad experiment can be further improved, we applied the RFI algorithm also to recover χ_γ from the $2\times\text{CO}_2$ rad experiment. We chose the $2\times\text{CO}_2$ rad experiment because as shown in Fig. 4 it has smaller forcing strengths than the maximum forcing strength for the 1% rad experiment – therefore nonlinearities should also not limit the recovery – but is expected to carry useful information over a larger range of the response spectrum. This expectation can be justified as follows (MacMartin
 225 and Kravitz, 2016). Taking the Laplace transform of Eq. (8) gives

$$\Delta\tilde{C}^{rad}(p) = \tilde{\chi}_\gamma(p)\Delta\tilde{T}(p) + \tilde{\eta}(p), \tag{10}$$

where the tilde denotes Laplace transformed functions. From Fig. 4 it is seen that for the 1% rad experiment the temperature ΔT behaves approximately as a linear function, which gives a Laplace transform $\Delta\tilde{T}(p)$ proportional to $1/p^2$. For the $2\times\text{CO}_2$ rad experiment, the temperature behaves approximately as a step function (ignoring the transient in the first 20 years), which
 230 gives a Laplace transform $\Delta\tilde{T}(p)$ proportional to $1/p$. This means that for the same χ_γ , the first term on the right-hand side of Eq. (10) – the “clean” response – decays to zero faster for the 1% rad experiment than for the $2\times\text{CO}_2$ rad experiment. Hence, assuming the same noise η for both cases, the response from the $2\times\text{CO}_2$ rad experiment gets buried in the noise only at larger p , meaning that this experiment carries useful information until higher rate values p than the response from the 1% rad experiment.

235 The response function $\chi_\gamma(t)$ recovered from the two types of experiments is shown in Fig. 5(a). As expected, the different experiments indeed result in different recoveries. Because we know from the analysis of Fig. 3 that nonlinearities do not limit

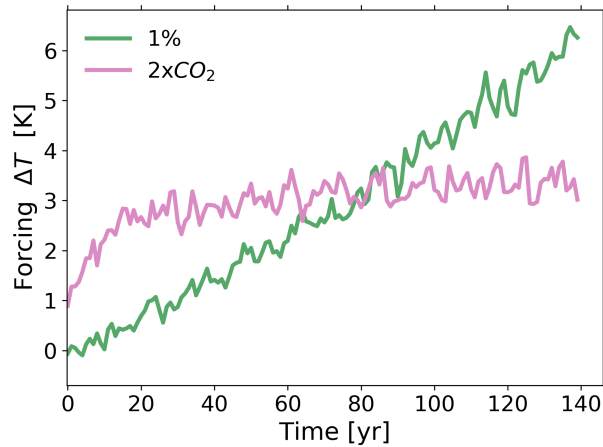


Figure 4. Forcing temperature $\Delta T(t)$ for 1% and $2\times\text{CO}_2$ rad experiments.

the recovery, the difference between the two response functions results probably from the difference in the quality of the data from the two types of experiments. To compare the robustness of each recovery, we analyze how well they predict the response from other experiments (Figs. 5(b) and (c)). If the response function is correctly recovered, it should be able to predict not only experiments with smaller but also experiments with higher forcing rate. Therefore, we include in the analysis also 1.5% and 2% rad experiments. To exclude errors that may be caused by nonlinearity, we take as a conservative estimate of the linear regime forcing strengths smaller than the final forcing strength at the end of the 1% rad experiment (which is approximately the maximum forcing strength; see temperature value at $t = 140$ years for the 1% rad experiment in Fig. 4). We take these values as an estimate of the linear regime because the 1% rad experiment has only 140 years so that no estimate for higher forcing strengths is available. Hence, for the 1.5% and 2% rad experiments the responses are expected to be reasonably predictable at least until the values marked with circles, where their respective forcing strengths reach this maximum forcing strength. All other experiments have forcing strengths smaller or equal to this maximum forcing strength so that they should be predictable for the whole time series.

Figure 5(b) shows the quality of the prediction using $\chi_\gamma(t)$ recovered from the 1% rad experiment. Visually, model response and prediction seem to have a comparable quality of agreement across the $1.1\times\text{CO}_2$, 0.5%, 0.75% and 1.5% rad experiments, while for the 2% and $2\times\text{CO}_2$ rad experiments there are larger discrepancies. For a quantitative analysis, we compute for the estimated linear regime the prediction error (7) for each experiment (right side of the plot). It is seen that the error varies from less than 10% for the 0.75% and 1.5% rad experiments to values between 10-20% for the 0.5%, 2% and $2\times\text{CO}_2$ rad experiments, and a significantly larger value of 57% for the $1.1\times\text{CO}_2$ rad experiment. To better understand these differences, it is important to note that as long as nonlinearities are small, experiments with higher forcing strength are expected to have smaller prediction error because they have higher SNR. This can be made plausible by considering that a perfectly recovered response function predicts a “clean” linear response (infinite SNR) with zero error, whereas the same response function can

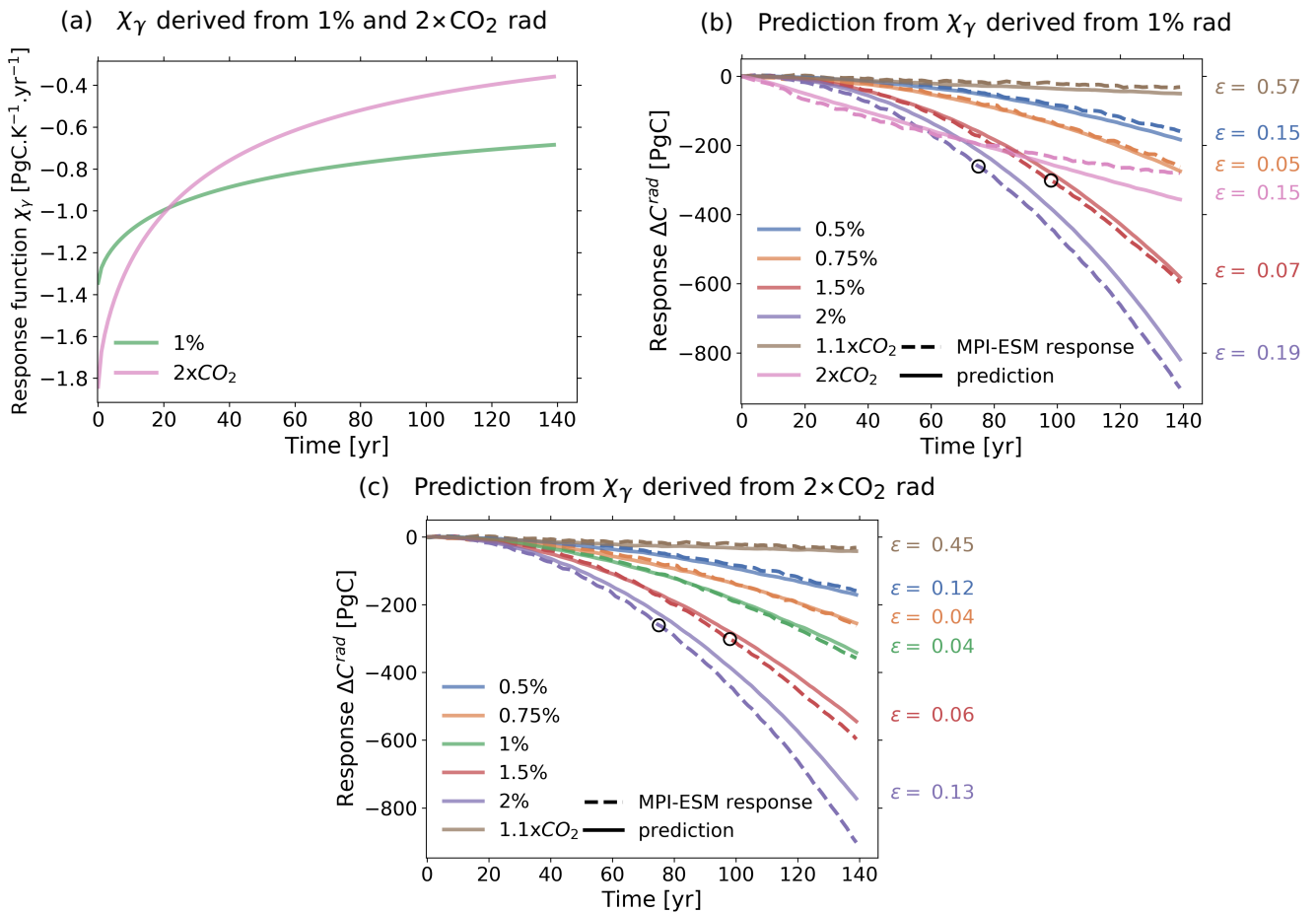


Figure 5. χ_γ recovered from 1% and 2xCO₂ rad experiments and prediction of model responses using these recoveries of χ_γ . Circles indicate the maximum value for which 1.5% and 2% responses are predictable according to the estimate of the linear regime (see text). At the right of subfigures (b) and (c) the prediction error (see Eq. (7)) is indicated for the different experiments, calculated for the 1.5% and 2% rad experiments by considering only values preceding the circles.



predict a noisy response only with some finite error. Therefore, if $\chi_\gamma(t)$ is well recovered, we expect large prediction errors for experiments with small forcing strengths such as the $1.1 \times \text{CO}_2$ rad – which is indeed the case –, but small errors for experiments with large forcing strengths but still well within the linear regime such as the $2 \times \text{CO}_2$ rad (compare the forcing strengths for the $2 \times \text{CO}_2$ rad experiment and the maximum forcing strength for the 1% rad experiment in Fig. 4). Since contrarily to the expectation the prediction error is not particularly small for the $2 \times \text{CO}_2$ rad experiment, probably the recovery of $\chi_\gamma(t)$ derived from the 1% rad experiment is not completely accurate and may still be further improved. As suggested above, such improvement may be achieved by taking data with better quality from the $2 \times \text{CO}_2$ rad experiment.

Figure 5(c) shows the quality of the prediction using $\chi_\gamma(t)$ recovered from the $2 \times \text{CO}_2$ rad experiment. As expected, results indicate an improvement in the recovery (compare to subfigure (b)). The prediction error decreases for all experiments present in both plots. In addition, it also decreases if we compare the prediction of the 1% rad response in subfigure (c) with that of the $2 \times \text{CO}_2$ rad response in subfigure (b).

This section therefore suggests two main conclusions: First, for $\chi_\gamma(t)$ the response seems to be approximately linear for temperature perturbations up to at least 6 K. Second, the overall improvement of the prediction in Fig. 5(c) compared to Fig. 5(b) confirms the expectation from the Laplace transform analysis that indeed the step-like $2 \times \text{CO}_2$ rad experiment carries more information on the response function than the 1% rad experiment. This suggests that step-like experiments may be more appropriate than the standard 1% experiment for the identification of linear response functions.

4 Generalized sensitivity χ_β

In this section we identify the linear response function χ_β (generalized β -sensitivity), defined by

$$\Delta C^{bgc}(t) = \int_0^t \chi_\beta(t-s) \Delta c(s) ds + \eta(t), \quad (11)$$

where now the response is $\Delta Y(t) := \Delta C^{bgc}(t)$ and the forcing is $\Delta f(t) := \Delta c(t)$, with $\Delta C^{bgc}(t)$ being the change in global land carbon found in the “bgc” experiment and $\Delta c(t)$ the change in atmospheric CO_2 .

That χ_β indeed generalizes β can be understood analogously to section 3 by considering that β is defined by

$$\beta(t) = \frac{\Delta C^{bgc}(t)}{\Delta c(t)} \stackrel{(11)}{=} \frac{1}{\Delta c(t)} \int_0^t \chi_\beta(t-s) \Delta c(s) ds, \quad (12)$$

for a negligible noise $\eta(t)$. Hence, $\chi_\beta(t)$ can be seen as a generalization of $\beta(t)$ and a property of the land carbon cycle that characterizes the response $\Delta C^{bgc}(t)$ to any time-dependent perturbation $\Delta c(t)$, as long as the perturbation strength is small.



Approaches to identify χ_β

Similarly to the last section, we identify $\chi_\beta(t)$ by several approaches to find the one that gives results with best quality. For
 285 this purpose, we consider in addition to Eq. (11) also alternative formulas to derive $\chi_\beta(t)$, each taking a different forcing. The
 identification is performed in three different ways:

1. Using CO_2 as forcing (see Eq. (11));
2. Using the logarithm of CO_2 as forcing:

$$\Delta C^{bgc}(t) = \int_0^t \chi_\beta^{\ln}(t-s) c_{PI} \ln\left(\frac{c(s)}{c_{PI}}\right) ds + \eta(t), \quad (13)$$

290 where now the forcing is $\Delta f(t) := c_{PI} \ln\left(\frac{c(t)}{c_{PI}}\right)$, with c_{PI} being the pre-industrial value for atmospheric CO_2 ;

3. Using Net Primary Production (NPP) as forcing:

$$\Delta C^{bgc}(t) = \int_0^t \chi_{NPP}(t-s) \Delta NPP(c(s)) ds + \eta(t). \quad (14)$$

The first approach is the same used throughout the paper: $\chi_\beta(t)$ is identified using the $\Delta c(t)$ forcing from Eq. (11).

For the second and third approaches, we take advantage of the fact that in the “bgc” setup, perturbations in atmospheric CO_2
 295 affect land carbon only via changes in photosynthetic productivity. Therefore, we use the CO_2 forcing only indirectly via its
 relationship to NPP. By doing this, the hope is to account for some of the nonlinear contributions to the response that arise from
 this relationship. The advantage of accounting for these nonlinear contributions is that one can recover the response function
 from experiments with perturbation strengths larger than those possible when not accounting for nonlinear contributions (as in
 the first approach). Experiments with larger perturbation strengths give responses with higher SNR, which makes it possible to
 300 recover the response function with better quality.

In the second approach (see Eq. (13)), we employ as forcing an explicit logarithmic expression describing the relationship
 between CO_2 and NPP (see e.g. Alexandrov et al., 2003). Such formula has the advantage that the expansion of the forcing in
 c gives

$$\Delta C^{bgc}(t) = \int_0^t \chi_\beta^{\ln}(t-s) \Delta c(s) ds + \mathcal{O}((\Delta c)^2) + \eta(t). \quad (15)$$

305 Taking Δc sufficiently small and comparing the result to Eq. (11) thus yields

$$\chi_\beta(t) = \chi_\beta^{\ln}(t). \quad (16)$$

Accordingly, the response function $\chi_\beta^{\ln}(t)$ from formula (13) gives as well the desired $\chi_\beta(t)$.

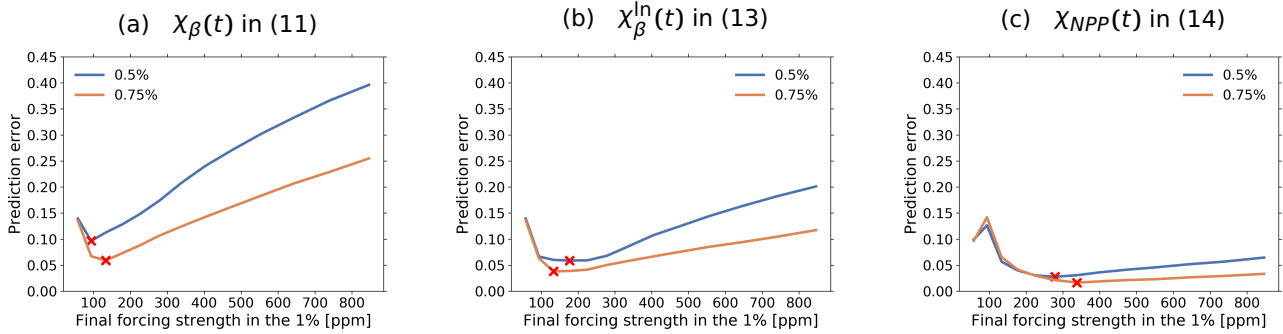


Figure 6. Prediction error (7) for the 0.5% and 0.75% bgc experiments obtained when using $\chi_{\beta}(t)$, $\chi_{\beta}^{\ln}(t)$ and $\chi_{NPP}(t)$ obtained from the 1% bgc experiment to predict the response. The error is shown as a function of the CO₂ final forcing strength.

In the third approach, we take directly the response to NPP (see Eq. (14)). Expanding the forcing $\Delta NPP(c)$ in c gives

$$\Delta C^{bgc}(t) = \int_0^t \chi_{NPP}(t-s) \frac{\partial NPP}{\partial c} \Big|_{c=c_{PI}} \Delta c(s) ds + \mathcal{O}((\Delta c)^2) + \eta(t). \quad (17)$$

310 Taking Δc sufficiently small and comparing the result to Eq. (11) yields

$$\chi_{\beta}(t) = \chi_{NPP}(t) \frac{\partial NPP}{\partial c} \Big|_{c=c_{PI}}. \quad (18)$$

Accordingly, by this approach we compute $\chi_{\beta}(t)$ in three steps: First, we identify the response function $\chi_{NPP}(t)$ using Eq. (14); second, we take the first derivative of NPP with respect to CO₂ at $c = c_{PI}$; third, we apply formula (18) to obtain $\chi_{\beta}(t)$ from $\chi_{NPP}(t)$.

315 Checking nonlinearities with the three approaches

Before analyzing the recovery of $\chi_{\beta}(t)$ employing the three approaches, one must verify that indeed these two additional approaches account for some of the nonlinearities in the response. If this is true, response formulas (13) and (14) should be able to predict the response to larger perturbation strengths than Eq. (11). To verify this expectation, in the following we compare the prediction error (7) by applying Eqs. (11), (13) and (14).

320 Figure 6(a) shows the prediction error for $\chi_{\beta}(t)$ recovered from the 1% bgc experiment with the first approach (Eq. (11)). The prediction is also computed via Eq. (11). The clear minima indicate the presence of strong nonlinearities for forcing strengths above around 100 ppm (94 ppm for the 0.5% and 133 ppm for the 0.75%). Therefore, in contrast to the case of χ_{γ} discussed in the last section, we see here that indeed one has to cope with the additional difficulty of nonlinearities.

325 Figure 6(b) shows the prediction error when using $\chi_{\beta}^{\ln}(t)$ recovered from the 1% bgc experiment with the second approach (Eq. (13)). To check how well nonlinearities are accounted for by taking the logarithmic forcing, the prediction is as well computed via Eq. (13). Compared to subfigure (a), we see a slight improvement in the results: The minima have smaller



prediction errors and the prediction errors increase at a slower rate for increasing final forcing strength. This indicates that indeed using the logarithm of CO_2 as forcing accounts for some of the nonlinearities in the response. Accordingly, one can make predictions with smaller error for larger forcing strengths using Eq. (13) instead of Eq. (11).

330 Figure 6(c) shows the prediction error for $\chi_{NPP}(t)$ recovered via Eq. (14) from the 1% bgc experiment (first step of the third approach). To check how well nonlinearities are accounted for by taking the NPP forcing, we employ as well Eq. (14) for the prediction. Here, we see a substantial improvement in the results. The response is almost completely linear, with very “flat” minima. This indicates that indeed a large part of the nonlinearity encountered in the response of the land carbon to changes in CO_2 can be explained by the nonlinear relationship between NPP and CO_2 . Accordingly, by employing Eq. (14) instead of
335 Eq. (11) one can predict the response of the land carbon until forcing strengths as high as 800 ppm with an error smaller than 10%.

χ_β and the quality of its recovery

So far, we have only considered the ability of Eqs. (11), (13) and (14) to predict the land carbon response. Now, we analyze how well the generalized sensitivity $\chi_\beta(t)$ can be identified by the three approaches. For the identification we took data from
340 the 1% bgc experiment until the CO_2 forcing strength reaches the first minimum for each case in Fig. 6: $\Delta c = 94$ ppm for the first approach (30 years); $\Delta c = 133$ ppm for the second approach (40 years); and $\Delta c = 279$ ppm for the third approach (70 years). Since $\Delta c = 279$ ppm is approximately the forcing strength for the $2\times\text{CO}_2$ bgc experiment and results from last section suggested that this type of experiment may carry more information for the identification, we employ the third approach also taking the $2\times\text{CO}_2$ bgc experiment. For the present application where the recovery is limited by nonlinearities, taking
345 the $2\times\text{CO}_2$ bgc experiment has the additional advantage that because its forcing strength has a constant value throughout the whole experiment, we can use the full time series (140 years). To compute the first derivative of NPP with respect to CO_2 (second step of the third approach), we fitted the function $NPP = NPP(c)$ to polynomials of order 4, 5 and 6, and then took the first derivative from the fits.

The results from the three approaches are shown in Fig. 7(a). At short time scales there is an overall agreement among all
350 recoveries with only small discrepancies. To be able to compare the results also for longer time scales, we extend the response functions recovered from the 1% bgc experiment – obtained from time series with 30, 40 and 70 years respectively for the first, second and third approaches – until 140 years (extensions are indicated by dotted lines). This can be done because with the RFI method we derive the response function from the ansatz (3), which formally gives the values of the response function for all times. The result is that all response functions recovered from the 1% bgc experiment present relatively small discrepancies
355 even at long time scales. Response functions derived from the $2\times\text{CO}_2$ bgc experiment with the third approach show a similar behaviour among themselves, but differ from the recoveries using the 1% bgc experiment. The reason for this difference will be investigated below.

To quantitatively compare the quality of the recoveries, we plotted in Fig. 7(b) the prediction error (7). Since the response functions were derived using different time series lengths, for a fair comparison we compute the error only at the minimal
360 time series length of 30 years (the time series length used for the first approach). Results show no large discrepancies among

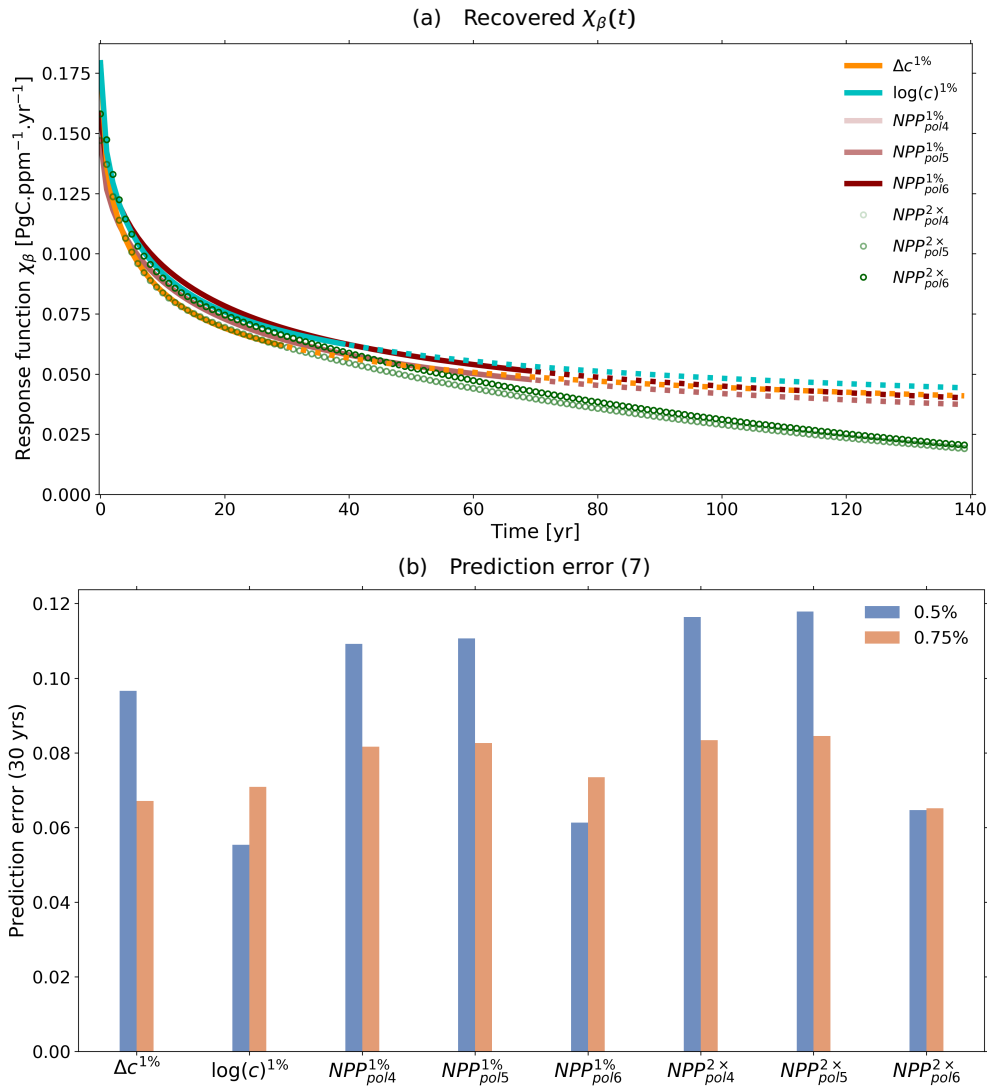


Figure 7. Response function $\chi_{\beta}(t)$ derived by the three approaches (subfigure (a)) and the respective prediction errors for the first 30 years of the response (subfigure (b)). $\Delta c^{1\%}$: recovery with first approach from 1% bgc experiment; $\log(c)^{1\%}$: recovery with second approach from the 1% bgc experiment; $NPP_{pol,x}^{1\%}$: recovery with third approach from the 1% bgc experiment using for the derivative a polynomial fit of order x ; $NPP_{pol,x}^{2\times}$: recovery with third approach from the $2\times CO_2$ bgc experiment using for the derivative a polynomial fit of order x . Continuous lines denote values of $\chi(t)$ that are within the time series length used for the recovery (30 years for $\Delta c^{1\%}$, 40 years for $\log(c)^{1\%}$ and 70 years for $NPP_{pol,x}^{1\%}$). Dotted lines denote extended parts of the response function, i.e. values not covered by the time series used for the recovery but obtained from the recovered spectrum using Eq. (3). Circles denote the response functions derived taking the full time series ($NPP_{pol,x}^{2\times}$). For more details see text.



the different approaches. For the third approach, there seems to be a small advantage in using a polynomial of order 6 for the computation of the derivative.

But results from subfigure (b) reflect only the quality of the recoveries at short time scales, for which anyway no large discrepancies were encountered in subfigure (a). To evaluate the quality of the recovery also at long time scales, one must take the extended version of the response functions that were derived from shorter time series. Since the only substantial difference at long time scales in Fig. 7(a) is found between the response functions recovered from the 1% and $2\times\text{CO}_2$ bgc experiments, we take for this analysis exemplarily only the response functions recovered with the first approach (1% bgc experiment) and the third approach ($2\times\text{CO}_2$ bgc experiment). By choosing the response function recovered with the first approach, we evaluate for the worst case scenario (where only 30 years are used for the recovery) how reliable predictions are for time scales longer than the time series used for recovery. In contrast, by choosing the response function recovered with the third approach from the $2\times\text{CO}_2$ bgc experiment, we check whether the different values at long time scales are actually an improvement in the recovery. As mentioned above, such improvement is expected because this response function was recovered taking the full time series (140 years).

Following the same procedure as in the last section, in Fig. 8 we show the quality of the prediction for different experiments using the aforementioned recoveries of $\chi_\beta(t)$. Subfigure (a) shows the results for the predictions calculated via Eq. (11) using $\chi_\beta(t)$ recovered with the first approach. We take as an estimate of the linear regime forcing strengths smaller than the forcing strength at the first minimum in Fig. 6(a). The response values corresponding to this forcing strength are marked in Fig. 8(a) with circles. It is seen that although $\chi_\beta(t)$ was recovered using a time series of only 30 years, it predicts the $1.1\times\text{CO}_2$ bgc experiment with only 3% error over 140 years. Other experiments are predicted within the linear regime with error smaller than 10% with exception of the 2% bgc experiment, for which the error is around 14%. Since the $2\times\text{CO}_2$ has a constant forcing strength outside the linear regime already from the beginning, its prediction fails as expected for the whole time series.

In subfigure (a) we could only evaluate the quality of the long time scales of $\chi_\beta(t)$ by the prediction of the $1.1\times\text{CO}_2$ bgc experiment, because this is the only experiment which has forcing strengths within the linear regime over the whole time series. To check the ability of $\chi_\beta(t)$ to predict also other experiments at long time scales, we account for some of the nonlinearity in the response by taking NPP instead of CO_2 as forcing (see discussion of Fig. 6). Therefore, we perform the prediction by employing Eq. (14) instead of Eq. (11). Since for employing Eq. (14) one needs $\chi_{NPP}(t)$ and not $\chi_\beta(t)$, we take the $\chi_\beta(t)$ derived with the first approach and compute $\chi_{NPP}(t)$ from it via Eq. (18). Because the conversion from $\chi_\beta(t)$ to $\chi_{NPP}(t)$ is a simple scaling, the time scales structure is maintained. Hence, we can evaluate the quality of the recovered $\chi_\beta(t)$ from the results given by the obtained $\chi_{NPP}(t)$. The prediction results computed via Eq. (14) with the obtained $\chi_{NPP}(t)$ are shown in subfigure (b). Because errors at the minima in Fig. 6(c) are not substantially smaller than those at the maximum final forcing strength, we take as an estimate of the linear regime all values smaller than the last value of NPP for the 1% bgc experiment (marked with circles in the responses). Once again it is seen that although $\chi_\beta(t)$ was recovered using a time series of 30 years, after conversion to $\chi_{NPP}(t)$ almost all experiments can be predicted with less than 10% error for the whole time series. The 1.5% and 2% bgc experiments are predicted with errors of 17% and 4% within the linear regime. Results from subfigures (a) and (b) therefore suggest that although nonlinearities do restrict the recovery from Eq. (11), taking experiments with forcing

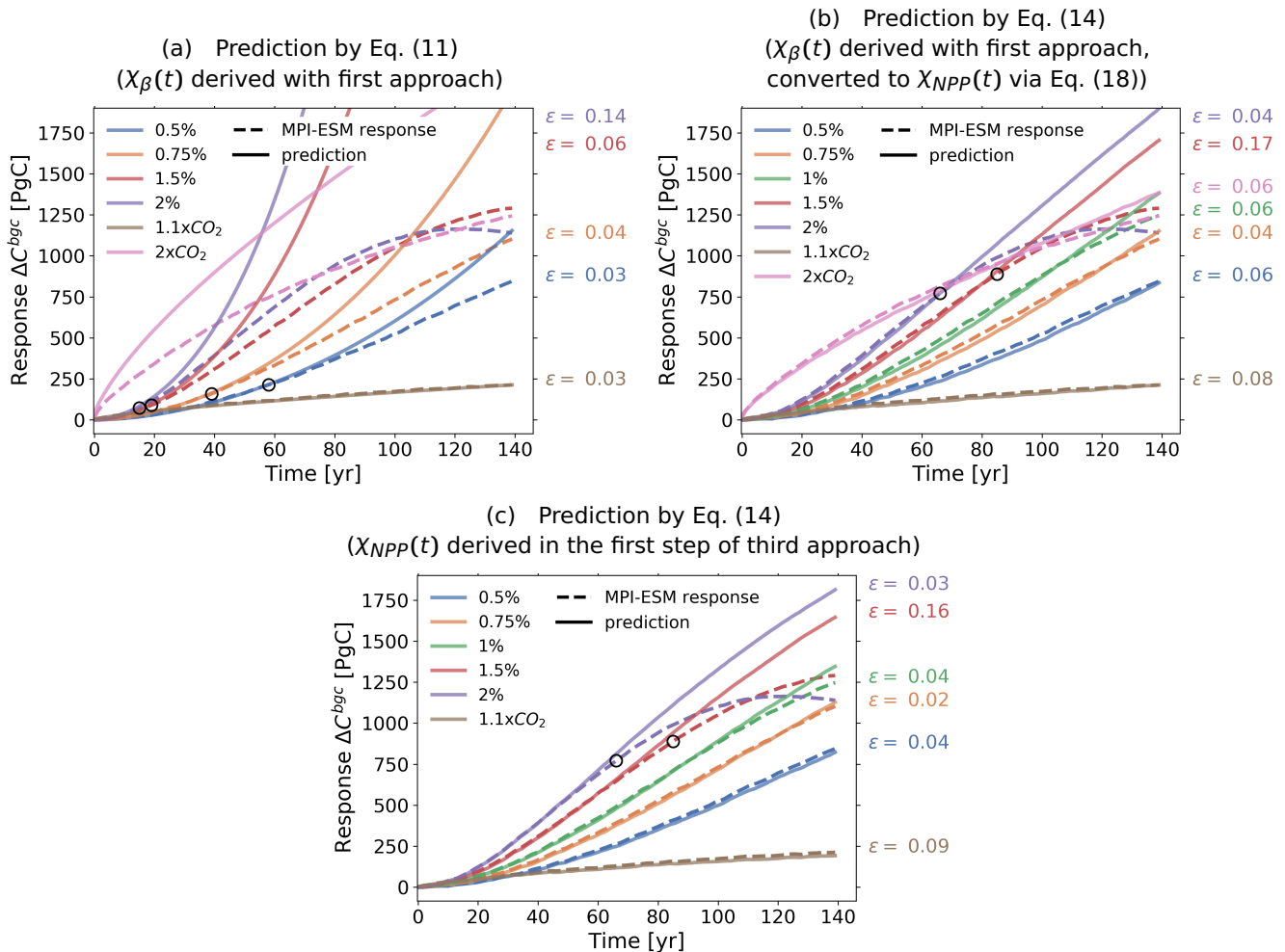


Figure 8. Prediction of model responses employing response functions derived with the first approach from the 1% bgc experiment (derived from data with 30 years length, but extended to 140 years) and with the third approach from the $2\times\text{CO}_2$ bgc experiment (derived from data with 140 years length). (a) Prediction by Eq. (11) taking the response function $\chi_{\beta}(t)$ derived from the 1% bgc experiment with the first approach. (b) Prediction by Eq. (14) taking the response function $\chi_{\beta}(t)$ derived from the 1% bgc experiment with the first approach and converted to $\chi_{NPP}(t)$ by Eq. (18). (c) Prediction by Eq. (14) taking the response function $\chi_{NPP}(t)$ derived in the first step of the third approach (see explanation after Eq. (18)) taking data from the $2\times\text{CO}_2$ bgc experiment. Continuous lines are predictions and dashed lines are responses from the MPI-ESM. Circles indicate the maximum value for which responses are predictable according to our estimate of the linear regime (see text). The values printed to the right of the plots are the prediction errors (see Eq. (7)) calculated for each experiment, considering when applicable only values preceding the circles.

strengths within the linear regime for the recovery leads to reliable prediction results even for times reasonably longer than the length of the time series from which the response function was recovered.



Finally, we investigate whether the different values seen in Fig. 7(a) for the $\chi_\beta(t)$ recovered from the $2\times\text{CO}_2$ bgc experiment indeed reflect a better quality of recovery. Following the same reasoning that led to subfigure (b), since in the third
400 approach $\chi_\beta(t)$ is obtained from a scaling of $\chi_{NPP}(t)$, we evaluate the quality of $\chi_\beta(t)$ from the results given by $\chi_{NPP}(t)$. Accordingly, in subfigure (c) we plot the prediction via Eq. (14) using the $\chi_{NPP}(t)$ recovered from the $2\times\text{CO}_2$ bgc experiment. As expected, the overall prediction indeed improves compared to subfigure (b). Individual prediction errors decrease for all experiments with exception of the $1.1\times\text{CO}_2$. Since the response functions used for subfigures (b) and (c) differ only at long
405 time scales, this improvement suggests that indeed obtaining $\chi_\beta(t)$ from the $2\times\text{CO}_2$ bgc experiment gives a better recovery over these time scales. Further, because all recoveries are similar at short time scales (see Fig. 7(a)), overall this recovery shows the best quality.

5 Spectrum of land carbon time scales

A response function obtained with high quality not only results in more accurate predictions, but may also provide valuable information about the internal dynamics of the system. For the case of $\chi_\beta(t)$, we find that the recovery with best quality gives
410 a relatively detailed description of the spectrum of land carbon time scales (see Eq. (3)). In this section, we investigate (i) the robustness of this result and (ii) the explanation for the structure of the obtained spectrum. The robustness of this detailed spectrum must be analyzed because, as explained in Part I, the problem to recover the spectrum of time scales from data is ill-posed so that in principle it is not clear to what extent the recovered spectrum can be trusted. To investigate this robustness, we check whether the main characteristics of the spectrum recovered by our RFI algorithm can as well be obtained by two
415 independent methods: a Gregory-plot approach (Gregory et al., 2004) and an approach that combines regional responses for the tropics and extra-tropics. Since the best recovery of $\chi_\beta(t)$ was obtained from the response to NPP for the $2\times\text{CO}_2$ bgc experiment, in our investigations we will study only this case.

Obtaining the detailed spectrum

But before we investigate the recovered spectrum, we demonstrate how such a detailed structure may arise from a better
420 recovery of the response function. In Fig. 9(a) we plot the spectrum $q(\tau)$ of the response function used for Fig. 8(b), i.e. $\chi_\beta(t)$ recovered with the first approach (see beginning of section 4) and converted to $\chi_{NPP}(t)$ via Eq. (18). Because the data used for the recovery have a relatively low quality – the response function was recovered from the 1% bgc experiment taken for only 30 years –, regularization filters out most of the SVD components of the spectrum in Eq. (4). Since the low-index SVD components that are not filtered out tend to be smooth (Hansen, 1989, 1990, see also Part I), the final result of this filtering is
425 the smooth spectrum seen in Fig. 9(a). Obviously, although this smooth spectrum is a sufficiently good approximation to make the predictions shown in Fig. 8(b), it is not very informative about the internal time scale structure. Instead, the spectrum of the response function $\chi_{NPP}(t)$ used for Fig. 8(c) has a more detailed structure (Fig. 9(b)). In this case, the higher quality of the data used for the identification ($2\times\text{CO}_2$ bgc experiment taken for 140 years) results in less filtering by regularization, thereby



430 revealing more details of the underlying spectrum. The result is a spectrum with two peak time scales, at around 4 and 100 years¹.

Checking the robustness of the spectrum via a Gregory-plot approach

Some trust in this result may be gained by constructing a type of “Gregory plot” (Gregory et al., 2004) for the land carbon (subfigure (c)) – which can be done because our $2\times\text{CO}_2$ bgc experiment is a step-like experiment. The idea here is to try to identify from an independent method important time scales in the response so that they can be compared against the spectrum
435 in subfigure (b). For this analysis, we plot the global land carbon against its first time derivative (this is the net land-atmosphere carbon flux). Using the $2\times\text{CO}_2$ bgc experiment where the forcing is constant, the first time derivative vanishes as the land carbon approaches a new equilibrium value. The rate at which the derivative changes can be associated to a time scale τ_i , which should show up with a large weight value q_i in the spectrum. Interestingly, the plot shows that the transient behaviour towards equilibrium develops approximately at two different rates: a higher rate from the starting point until around 3520
440 PgC, and a lower rate from 3520 PgC onwards. To determine these rate values, we fitted a linear function $dC/dt = a + bC^{\text{bgc}}$ for each of these two ranges of the land carbon. Then, from each rate value b we computed a time scale by $\tau = -1/b$. The computed time scales taking one standard deviation into account are shown by the two ranges highlighted in subfigure (b). As seen, also the Gregory plot reveals a time scale structure dominated by two time scales. While the shortest time-scale peak of the spectrum partially overlaps with the corresponding time-scale range from the Gregory plot, the longest time-scale peak is
445 almost perfectly matched². This result suggests that indeed the recovered spectrum reflects internal characteristics of the global response of the land carbon cycle.

Checking the robustness of the spectrum via regional response functions

The robustness of this detailed spectrum can be further checked by a different method. In the following, we test this robustness by checking the consistency between the time scales of global and regional carbon responses.

450 To study regional carbon responses we considered two regions: Tropics and extra-tropics. Tropics were defined as the region between latitudes 30° south and 30° north, and extra-tropics as the remaining part of the globe. We then determined separately the linear response functions that characterize the land carbon response to NPP in the tropics and extra-tropics,

¹We ignore the negative values obtained for time scales smaller than 1 year (data time step) and larger than 140 years (time series length) because spectral contributions at time scales much longer or much shorter than the time scales covered by data cannot be correctly recovered. Yet, as demonstrated in Appendix D, their wrong recovery does not strongly affect the recovered response function so that they can be safely ignored. Other slightly negative values between the two peaks are probably small recovery errors that inevitably appear as a consequence of ill-posedness and the filtering by regularization (such slightly negative values have also been observed in recovered spectra shown in Appendix E).

²A possible reason for the better matching at long time scales is that these time scales contribute to the response at short and long times, while contributions at short time scales decay rapidly and therefore contribute only at short times. This gets clear by considering for example a response function $\chi(t) = a_1 e^{-t/\tau_1} + a_2 e^{-t/\tau_2}$, $\tau_2 \gg \tau_1$. While $a_2 e^{-t/\tau_2}$ contributes to $\chi(t)$ at small and long times, $a_1 e^{-t/\tau_1}$ contributes only at small times.

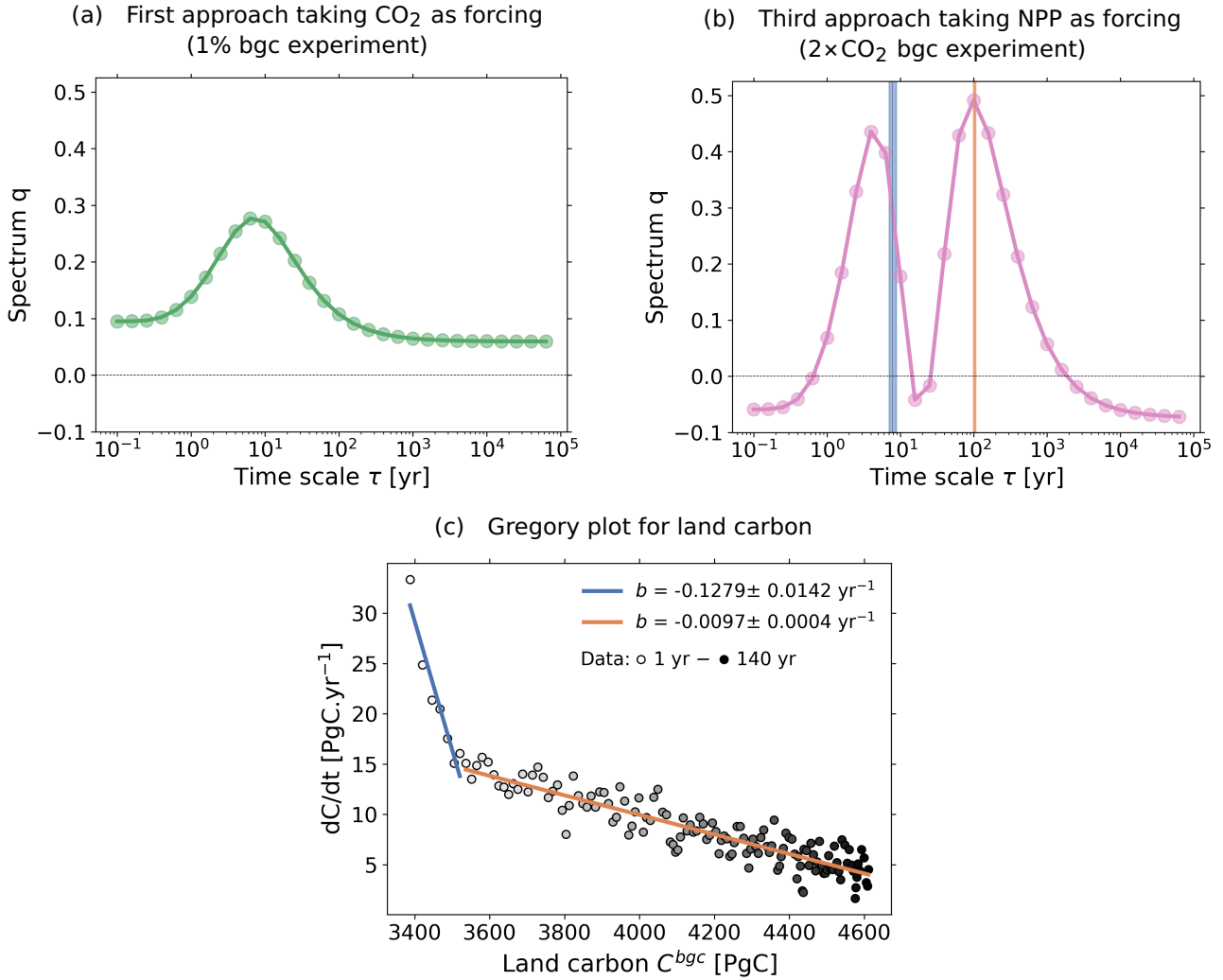


Figure 9. Spectra associated to χ_{NPP} derived with different resolutions and Gregory plot for land carbon. (a) Spectrum derived with the first approach (taking CO₂ as forcing) from the 1% bgc experiment; (b) Spectrum derived with the third approach (taking NPP as forcing) from the 2×CO₂ bgc experiment; (c) “Gregory plot” for land carbon. Dots are the data, with the color scale from white to black indicating the evolution from 1 to 140 years. Values of b indicate the rate at which the time derivative of land carbon changes with respect to the land carbon itself. Ranges of time scales corresponding to each rate accounting for one standard deviation are shown in subfigure (b).

defined respectively by

$$\Delta C^{bgc,tr}(t) = \int_0^t \chi_{NPP}^{tr}(t-s) \Delta NPP^{tr}(s) ds + \eta^{tr}(t), \quad (19)$$

$$455 \quad \Delta C^{bgc,et}(t) = \int_0^t \chi_{NPP}^{et}(t-s) \Delta NPP^{et}(s) ds + \eta^{et}(t). \quad (20)$$

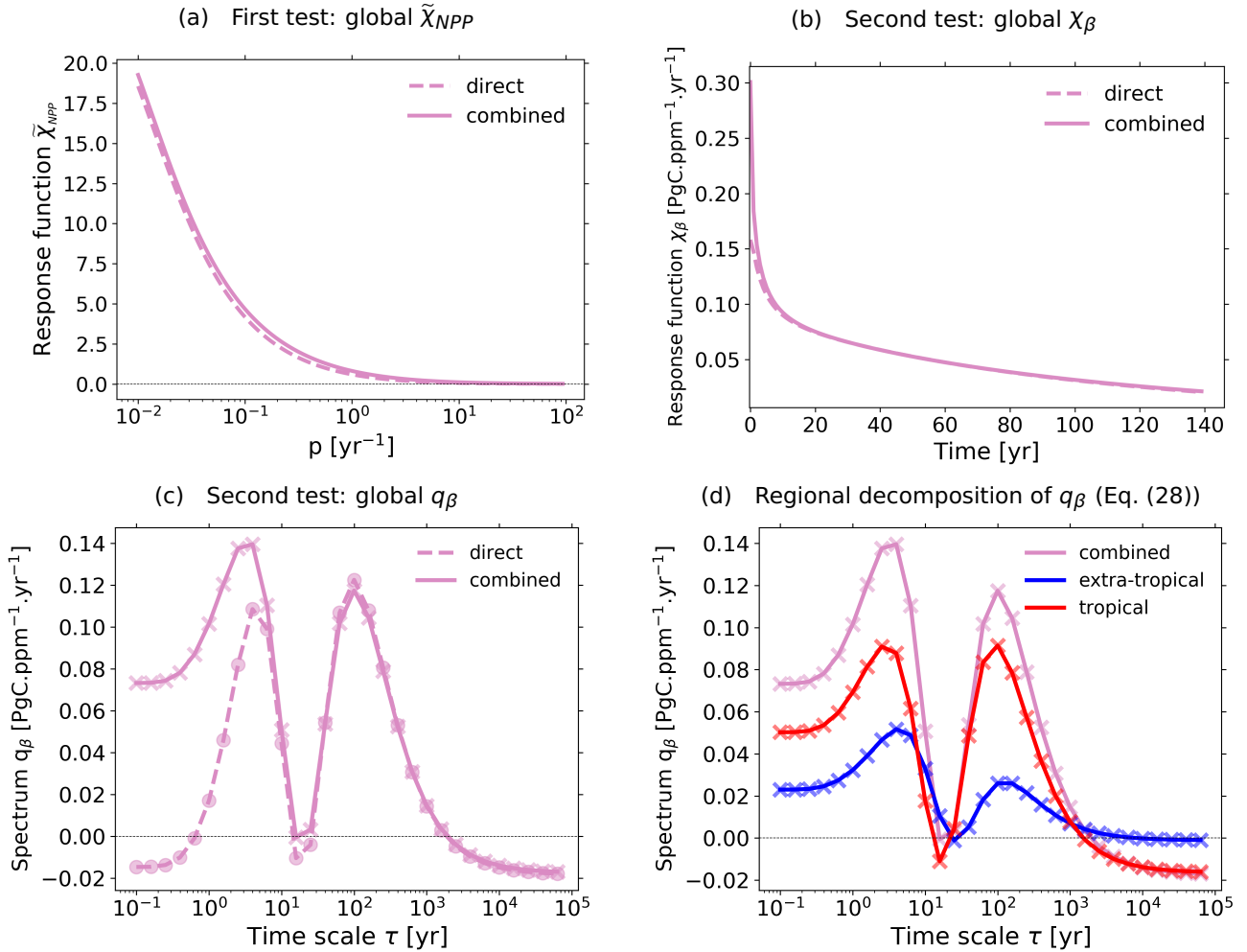


Figure 10. Investigation of the land carbon response in the tropics and extra-tropics and how the regional response functions combine to the global response functions. The analysis is based on the $2\times\text{CO}_2$ bgc experiment. (a) Laplace transform $\tilde{\chi}_{NPP}(p)$ of global $\chi_{NPP}(t)$ obtained directly from the global carbon response and from combining the tropical and extra-tropical response functions; (b) $\chi_{\beta}(t)$ obtained directly from the global carbon response and from combining the tropical and extra-tropical response functions; (c) As (b) but for $q_{\beta}(\tau)$; (d) Decomposition of $q_{\beta}(\tau)$ into tropical and extra-tropical spectra (Eq. (28)). In (c) and (d) the dots and crosses indicate the computed values, while the connecting lines are only inserted to guide the eye. For more details see text.

The data were taken once more from the $2\times\text{CO}_2$ bgc experiment.

Before assessing the robustness of the spectrum, we check the consistency between the regional and global response functions. In this test, we show that the global response function χ_{NPP} can be reconstructed by combining χ_{NPP}^{tr} and χ_{NPP}^{et} . For



this purpose, we write the global land carbon as the sum of the land carbon in the tropics and extra-tropics:

$$460 \quad \Delta C^{bgc}(t) = \Delta C^{bgc,tr}(t) + \Delta C^{bgc,et}(t). \quad (21)$$

Plugging Eqs. (14), (19) and (20) in Eq. (21) and recognizing that $\eta(t) = \eta^{tr}(t) + \eta^{et}(t)$ gives

$$\int_0^t \chi_{NPP}(t-s) \Delta NPP(s) ds = \int_0^t \chi_{NPP}^{tr}(t-s) \Delta NPP^{tr}(s) ds + \int_0^t \chi_{NPP}^{et}(t-s) \Delta NPP^{et}(s) ds. \quad (22)$$

Applying a Laplace transform to both sides of Eq. (22) and reorganizing the resulting equation gives

$$\tilde{\chi}_{NPP}(p) = \frac{\tilde{\chi}_{NPP}^{tr}(p) \Delta \tilde{NPP}^{tr}(p) + \tilde{\chi}_{NPP}^{et}(p) \Delta \tilde{NPP}^{et}(p)}{\Delta \tilde{NPP}(p)}. \quad (23)$$

465 Therefore, the Laplace transformed $\tilde{\chi}_{NPP}(p)$ can be obtained from combining the NPP forcings and the response functions for the tropics and extra-tropics. Hence, if the response functions are correctly recovered by the RFI algorithm, Eq. (23) should hold at least approximately. In order to check this, we computed the Laplace transforms analytically by approximating the NPP forcings by step functions (since we take the $2 \times \text{CO}_2$ bgc experiment), and using Eq. (3) for the response functions. Figure 10(a) shows the quality of the result. The small discrepancy between $\tilde{\chi}_{NPP}(p)$ obtained from the global carbon response and
 470 from combining the regional responses can be at least partially explained by the approximation error made to represent the forcings by a step function.

We now check the robustness of the land carbon spectrum by combining $\chi_{NPP}^{tr}(t)$ and $\chi_{NPP}^{et}(t)$ to obtain $\chi_{\beta}(t)$ and thereby $q_{\beta}(\tau)$. To this end, we first obtain the tropical $\chi_{\beta}^{tr}(t)$ and extra-tropical $\chi_{\beta}^{et}(t)$ by applying Eq. (18):

$$\chi_{\beta}^{tr}(t) = \left. \frac{\partial NPP^{tr}}{\partial c} \right|_{c=c_{PI}} \chi_{NPP}^{tr}(t), \quad (24)$$

$$475 \quad \chi_{\beta}^{et}(t) = \left. \frac{\partial NPP^{et}}{\partial c} \right|_{c=c_{PI}} \chi_{NPP}^{et}(t). \quad (25)$$

Using the obtained response functions, one can now write Eq. (11) for global, tropical and extra-tropical carbon. Plugging the result into Eq. (21) gives

$$\int_0^t \chi_{\beta}(t-s) \Delta c(s) ds = \int_0^t [\chi_{\beta}^{tr}(t-s) + \chi_{\beta}^{et}(t-s)] \Delta c(s) ds. \quad (26)$$

Hence, one can infer that

$$480 \quad \chi_{\beta}(t) = \chi_{\beta}^{tr}(t) + \chi_{\beta}^{et}(t). \quad (27)$$

Therefore, the global response function $\chi_{\beta}(t)$ can be obtained from $\chi_{\beta}^{tr}(t)$ and $\chi_{\beta}^{et}(t)$. But in addition, since $\chi(t)$ is given by Eq. (3), Eq. (27) implies that one can also obtain the global spectrum $q_{\beta}(\tau)$ by combining the regional spectra:

$$q_{\beta}(\tau) = q_{\beta}^{tr}(\tau) + q_{\beta}^{et}(\tau). \quad (28)$$



Therefore, using the recovered response functions for tropical and extra-tropical carbon one can obtain the global response
485 function χ_β and its associated spectrum q_β . Accordingly, in this test we check Eqs. (27) and (28). For the calculation of the
derivatives in Eqs. (24) and (25) we fitted $NPP^{tr} = NPP^{tr}(c)$ and $NPP^{et} = NPP^{et}(c)$ once again by a polynomial of
order 6 (which obtained the best results for global NPP in Fig. 7(b)) and took the derivatives from the fits. For $\chi_\beta(t)$ we used
the recovery with best quality from Fig. 7 (“NPP^{2x}”). The spectra $q_\beta(\tau)$, $q_\beta^{tr}(\tau)$ and $q_\beta^{et}(\tau)$ are obtained by scaling the spec-
tra from $\chi_{NPP}(t)$, $\chi_{NPP}^{tr}(t)$ and $\chi_{NPP}^{et}(t)$ by the respective derivatives $\left. \frac{\partial NPP}{\partial c} \right|_{c=c_{PI}}$, $\left. \frac{\partial NPP^{tr}}{\partial c} \right|_{c=c_{PI}}$ and $\left. \frac{\partial NPP^{et}}{\partial c} \right|_{c=c_{PI}}$.
490 Results are shown for χ_β in Fig. 10(b) and for q_β in Fig. 10(c). As seen in subfigure (b), the reconstruction matches almost
perfectly the values of χ_β for times beyond about 20 years. Likewise, the spectrum q_β is almost perfectly reconstructed for time
scales above 6 years, with a slight discrepancy between 15 and 25 years (see Fig. 10(c)). A larger disagreement is seen below
20 years for χ_β and below 6 years for q_β . One of the reasons is that only little information is available for time scales smaller
than 1 year because this is the time step taken for the data. However, Appendix D shows that time scales much shorter than the
495 time step affect only $\chi(0)$. The main reason for the disagreement is that high frequencies (and thus small time scales) are the
most problematic to recover due to the ill-posedness of the problem that obscures the signal particularly at high frequencies.

Despite the disagreement at small time scales, Figs. 10(b) and (c) add confidence that: 1) The response functions for global,
tropical and extra-tropical carbon can be trusted over mid-to-long time scales (Fig. 10(b)); and 2) the two-peak spectrum
obtained for global land carbon indeed characterizes the response, since its computation from two independent approaches
500 (combining regional spectra in Fig. 10(c) and the Gregory plot in Fig. 9(c)) yield similar results with characteristic time scales
matching the peaks of the spectrum.

Investigating the two-peak structure of the spectrum

The reasons for the two-peak structure of the land carbon spectrum are conceivable. In principle, one possibility could be that
the short time scales reflect the carbon dynamics in the tropics, a region with higher temperatures and thus larger heterotrophic
505 respiration rates (see e.g. Raich and Potter, 1995), while the long time scales may originate from the carbon dynamics in the
extra-tropics, where respiration rates are smaller due to lower temperatures. This hypothesis may be checked by examining
Fig. 10(d), which shows the contribution from the tropics and the extra-tropics to the land carbon spectrum (Eq. (28)). But as
seen, the two peaks arise both in the tropical and in the extra-tropical spectrum, so that one cannot attribute each peak to a
particular region. Therefore, this cannot be the explanation.

510 An alternative hypothesis is that the different peak time scales originate from the very different characteristic time scales of
functionally different elements in the land carbon cycle such as leaves, wood, litter and soil. In the following we investigate
whether this hypothesis can explain the two-peak structure.

For this purpose, we split the land carbon pools of the MPI-ESM into two groups (see Fig. 11). In the first group are the
pools whose dynamics is governed by fast processes such as shedding and decomposition of leaves, thus the pools that respond
515 at short time scales. These are the pools representing non-woody tissues in living vegetation (leaves, fine roots, sugars, and
starches) and the associated litter. In the second group are the pools with dynamics determined by slow processes such as the



decomposition of woody plant parts, hence the pools that respond at long time scales. These are the pools representing the wood in stems and coarse roots, the associated litter pools, and the soil carbon (humus).

Now, we separate the land carbon spectrum into contributions arising from each of these two groups. The land carbon response can be described as the sum of the collective responses from the pools with fast and those with slow dynamics:

$$\Delta C^{bgc}(t) = \Delta C^{bgc,f}(t) + \Delta C^{bgc,s}(t). \quad (29)$$

In the linear response framework, the response of each term to NPP is given by

$$\int_0^t \chi_{NPP}(t-s) \Delta NPP(s) ds = \int_0^t \chi_{NPP}^f(t-s) \Delta NPP(s) ds + \int_0^t \chi_{NPP}^s(t-s) \Delta NPP(s) ds, \quad (30)$$

which implies

$$\chi_{NPP}(t) = \chi_{NPP}^f(t) + \chi_{NPP}^s(t). \quad (31)$$

Finally, assuming that each response function in Eq. (31) is described by Eq. (3), we obtain the separation of the land carbon spectrum in terms of the contribution from each pool group:

$$q_{NPP}(\tau) = q_{NPP}^f(\tau) + q_{NPP}^s(\tau). \quad (32)$$

Hence, if our hypothesis is correct, then the peak at short time scales should be explained by q_{NPP}^f and the peak at long time scales should be explained by q_{NPP}^s .

To proceed with the analysis we now need to obtain the spectra q_{NPP}^f and q_{NPP}^s . When investigating the tropical and extra-tropical land carbon, we obtained each regional spectrum individually by applying the RFI algorithm to the data from the tropical and extra-tropical responses. In principle one could proceed in the same way to separate contributions from the two pool groups, but, as will get clear below, this approach introduces slight inconsistencies between the separate recoveries that makes a quantitative comparison of the two contributions less reliable than the alternative method that we use in the following to separate the fast and slow components of q_{NPP} .

The idea of this alternative approach is the following. Numerically the land carbon spectrum is given by the regularized solution (4), i.e.

$$q_{NPP,\lambda} = \sum_{i=0}^{M-1} \frac{\sigma_i^2}{\sigma_i^2 + \lambda} \frac{\mathbf{u}_i \bullet \Delta C^{bgc}}{\sigma_i} \mathbf{v}_i, \quad (33)$$

where the regularization parameter λ is determined by the RFI algorithm. The land carbon response ΔC^{bgc} is given by the sum (29) of the responses from the pools with fast and those with slow dynamics. Entering Eq. (29) into Eq. (33) yields

$$q_{NPP,\lambda} = \sum_{i=0}^{M-1} \frac{\sigma_i^2}{\sigma_i^2 + \lambda} \frac{\mathbf{u}_i \bullet (\Delta C^{bgc,f} + \Delta C^{bgc,s})}{\sigma_i} \mathbf{v}_i = q_{NPP,\lambda}^f + q_{NPP,\lambda}^s. \quad (34)$$

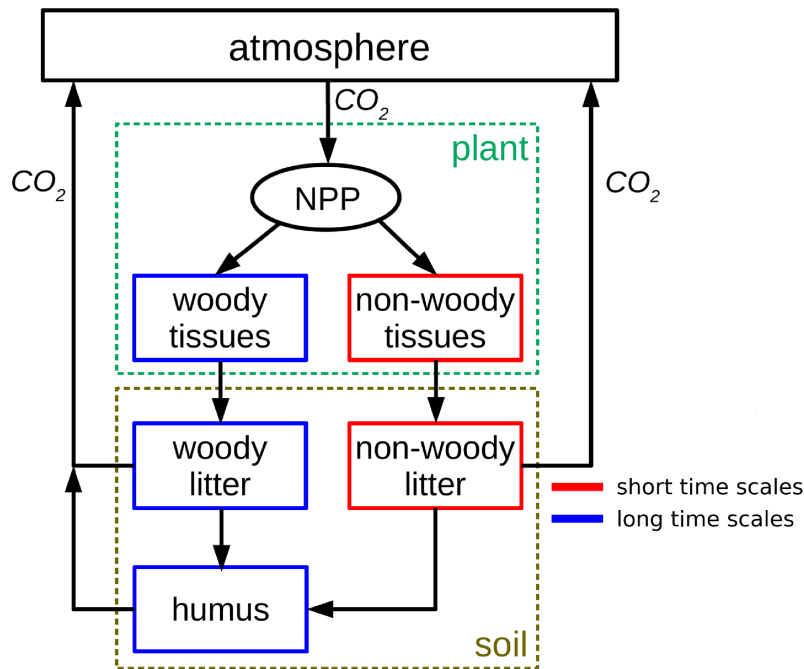


Figure 11. Simplified pool scheme of the land carbon cycle in the MPI-ESM (see Appendix A) with pools split into two groups according to the characteristic time scales underlying their dynamics.

Therefore, by deriving the spectra $q_{NPP,\lambda}^f$ and $q_{NPP,\lambda}^s$ using the same regularization parameter λ employed for the land carbon spectrum $q_{NPP,\lambda}$, we can in principle accurately reconstruct $q_{NPP,\lambda}$ from $q_{NPP,\lambda}^f$ and $q_{NPP,\lambda}^s$.

545 By obtaining $q_{NPP,\lambda}^f$ and $q_{NPP,\lambda}^s$ in this way and combining them via Eq. (32) we show that indeed $q_{NPP,\lambda}$ can be very accurately reconstructed (Fig. 12(a)). This approach leads as well to an almost perfect reconstruction of the response function χ_{NPP} via Eq. (31), as shown in Fig. 12(b). Compared to our previous approach employed to reconstruct the global spectrum from the regional spectra (Eq. (28)), this alternative approach gives a more accurate reconstruction because it takes the same regularization parameter λ for all $q_{NPP,\lambda}$, $q_{NPP,\lambda}^f$, and $q_{NPP,\lambda}^s$, in contrast to the previous approach where λ was separately
 550 calculated by the RFI algorithm for each spectrum in Eq. (28).

Now, the question is whether the spectra q_{NPP}^f and q_{NPP}^s can indeed explain each peak in the land carbon spectrum q_{NPP} . To check this, in Fig. 12(c) we plot the three spectra. As seen, clearly the peak at short time scales of the land carbon spectrum arises mostly from the large peak in the fast-dynamics spectrum, while the peak at long time scales follows closely the large peak in the slow-dynamics spectrum. This result thus indicates that our hypothesis is correct, so that indeed the two-peak
 555 spectrum originates from the different characteristic time scales of functionally different elements in the land carbon cycle.

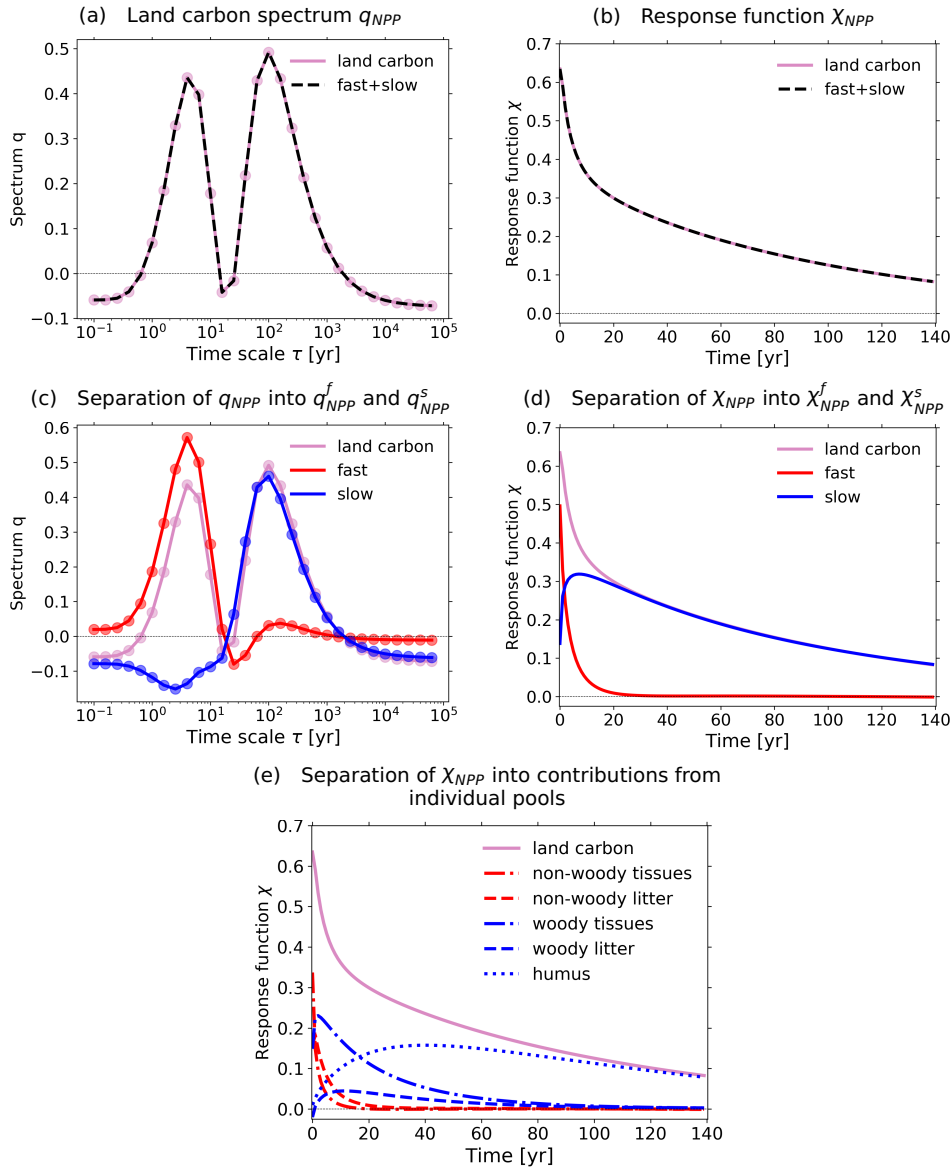


Figure 12. Investigation of the contribution from the pools with fast dynamics (non-woody pools) and those with slow dynamics (woody and humus pools) to the land carbon spectrum. The analysis is based on the $2\times\text{CO}_2$ bgc experiment. (a) Land carbon spectrum q_{NPP} and its reconstruction via Eq. (32) from the fast and slow components; (b) response function χ_{NPP} and its reconstruction via Eq. (31) from the response functions for the fast and the slow components; (c) separation of spectrum q_{NPP} into q_{NPP}^f and q_{NPP}^s ; (d) separation of response function χ_{NPP} into χ_{NPP}^f and χ_{NPP}^s ; (e) separation of χ_{NPP} into contributions from the individual pools. For more details see text.



More insight into the dynamics of the land carbon can be gained by analyzing the different contributions to the response function χ_{NPP} shown in Figs. 12(d) and 12(e). Subfigure (d) shows the contribution of the pools with fast dynamics χ_{NPP}^f and that of the pools with slow dynamics χ_{NPP}^s . We see that χ_{NPP}^f only dominates the response at times smaller than about 2 years. Further, for times larger than 25 years only χ_{NPP}^s contributes to the response. In subfigure (e) we further separate the
560 response functions into the contributions from the individual pools, i.e.

$$\chi_{NPP}^f(t) = \chi_{NPP}^{nwt}(t) + \chi_{NPP}^{nwl}(t), \quad (35)$$

$$\chi_{NPP}^s(t) = \chi_{NPP}^{wt}(t) + \chi_{NPP}^{wl}(t) + \chi_{NPP}^h(t), \quad (36)$$

where χ_{NPP}^{nwt} is the response function for the non-woody tissues in living vegetation, χ_{NPP}^{nwl} for non-woody litter, χ_{NPP}^{wt} for woody tissues in living vegetation, χ_{NPP}^{wl} for woody litter, and χ_{NPP}^h for the humus pool. This more detailed separation
565 shows that for long times the humus pool starts to dominate the response so that at times larger than 100 years it gives the only contribution.

6 Summary, discussion and outlook

Although the γ and β values introduced by Friedlingstein et al. (2003) provide a useful framework for model intercomparison, they only characterize the sensitivity of a model for a particular perturbation scenario. Instead, one would like to characterize the
570 sensitivity as such. The dependence of γ and β on the considered scenario arises because of the internal memory of the system, i.e. because of the dependence of the response on past values of the perturbation. When the memory is taken into account, linear response functions arise as natural generalization of the γ and β sensitivities. But a fundamental step for applying this generalized framework is to identify the appropriate linear response functions. In Part I, we developed a method to identify linear response functions from data using only information from an arbitrary perturbation experiment and a control simulation.
575 In that study, the robustness of the method in the presence of noise and nonlinearity was demonstrated in applications to data from perturbation experiments performed with a toy model.

Generalized land carbon sensitivities in the MPI-ESM

In the present study, we demonstrated that our RFI method can as well be employed to derive response functions from C⁴MIP data. Here, we identified for the MPI-ESM, using data from standard 1% experiments, the land carbon generalized sensitivities
580 χ_γ and χ_β , i.e. the linear response functions that generalize the γ - and β -sensitivities for land carbon. The robustness of the identified generalized sensitivities was demonstrated by their ability to predict the response from experiments not used for the identification (sections 3 and 4). With the aid of additional experiments, we estimated the linear regime that gives the range of forcing strengths for which each generalized sensitivity can predict model responses. For χ_γ , results indicate a linear response at least until the end of the 1% experiment, corresponding to temperature perturbations of around 6 K. For χ_β , the estimate is
585 for CO₂ perturbation strengths up to 100 ppm. In addition, we analyzed different approaches that may be employed to improve the quality of the recovery of the response functions. For χ_γ , taking the response from a 2×CO₂ experiment demonstrated to



give smaller prediction errors for every response evaluated, suggesting that this type of experiment gives also a better recovery. For χ_β , we used the knowledge of the relationship between NPP and CO_2 to account for some of the nonlinearities in the response. We found that nonlinearities can to a large extent be explained by the nonlinear relationship between NPP and CO_2 :
590 By using NPP instead of CO_2 as forcing an approximately linear response is found over the whole 1% experiment, i.e. until CO_2 perturbations of about 850 ppm. In addition, this approach yielded the best recovery for χ_β . Evidences for this conclusion are the quality of its prediction and the detailed spectrum it yields for the response.

Spectrum of land carbon time scales

Obtaining the spectrum of the response is an additional advantage of the RFI method. Most methods in the literature either
595 recover $\chi(t)$ pointwise – and therefore do not give the spectrum –, or try to fit it with few exponents without accounting for ill-posedness, which does not give reliable results for the spectrum (see e.g. the famous example from Lanczos, 1956, p. 272). In the application to the MPI-ESM, obtaining the spectrum has proven advantageous for two reasons. First, it allows to formally extend the recovery of the response function beyond the time range of the length of the underlying time series. Results from such an extension (Figs. 8(a) and (b)) demonstrated that the recovered response function contains information on
600 times reasonably longer than the time series length used for the recovery.

Second, the spectrum gives valuable insight into the internal dynamics of the system. In particular, for our application the spectrum gives the most relevant time scales for the land carbon response on a global or regional level. The spectrum associated with the best recovery of χ_β showed two peak time scales for the global response: One around 4 and another around 100 years (section 5).

605 To obtain evidence for the robustness of this result, we showed that it is possible to reconstruct the global spectrum from the recovered tropical and extra-tropical spectra (see Fig. 10(c)), and that similar time scale ranges can be obtained via a “Gregory plot” approach (see Fig. 9(b) and (c)). Further, we demonstrated that the recovered tropical and extra-tropical response functions combine to the identified global response functions, indicating consistency between regional and global recovery (see Fig. 10(a) and (b)).

610 We then proceeded to investigate the reason for the two-peak structure of the spectrum. To this end, we separated the land carbon response into the response from pools with fast dynamics (non-woody vegetation tissues and associated litter) and the response from pools with slow dynamics (woody vegetation tissues, woody litter, and humus). By analyzing the spectrum for each of these responses we showed that the peak at short time scales of the land carbon spectrum arises mostly from the contribution of the pools with fast dynamics, while the peak at long time scales follows closely the contribution from the pools with slow dynamics. This investigation therefore suggests that the two-peak spectrum results from the different contributions of functionally different elements of the land carbon cycle. Analysis of the response functions showed that the pools with fast dynamics dominate the land carbon response only for times below 2 years. Further, for times larger than 25 years only the pools with slow dynamics contribute to the response, and from 100 years onwards the contribution comes solely from the humus pool.



620 We remark that results for the spectrum should be always interpreted with care, since deriving the spectrum may be a more
complicated problem than deriving the response function. This is partially explained by the degree of ill-posedness of each
problem. In deriving the response function from Eq. (1), one is solving a deconvolution problem, which is known to be ill-
posed because of the smoothing property of the convolution operator (e.g., Landl et al., 1991; Bertero et al., 1995; Hansen,
2002). On the other hand, by deriving the spectrum from Eqs. (1) and (3), one is solving not only a deconvolution (Eq. (1))
625 but also a type of inverse Laplace transform (to obtain the spectrum from the response function (3)), which is known to be
extremely ill-posed because of the smoothing property of the Laplace operator (e.g., McWhirter and Pike, 1978; Istratov and
Vyvenko, 1999). As a result, deriving $q(\tau)$ from the data $\Delta Y(t)$ involves two smoothing operations, namely the Laplace
transform and convolution, whereas deriving $\chi(t)$ from $\Delta Y(t)$ involves only convolution, so that the problem of finding $q(\tau)$
may be more ill-posed than that of finding $\chi(t)$. This difficulty was exemplified by results from appendices D and E, which
630 discuss cases where the response function can be perfectly recovered but the recovered spectrum is relatively poor.

Another worthwhile comment is that, in comparison to the widely used assumption that the spectrum can be described by
only a few exponents (Maier-Reimer and Hasselmann, 1987; Enting and Mansbridge, 1987; Enting, 1990; Joos et al., 1996;
Pongratz et al., 2011; Joos et al., 2013; Colbourn et al., 2015; Lord et al., 2016), our assumption of a continuous spectrum
(ansatz (3)) has some advantages. First, by our approach one circumvents the complication of determining the number of
635 exponents. This leads to a linear problem and thereby to a more transparent method (see Part I, section 3.1). Second, our ansatz
better describes the expectation that variables integrated over many different climate zones are composed by a large range of
time scales. If, in contrast to these expectations, the underlying spectrum has only few time scales, results in Appendix E show
that our approach may still yield a reasonable recovery.

Outlook

640 In this study we investigated the generalized γ - and β -sensitivities that solve the scenario dependence problem noted e.g. by
Gregory et al. (2009) and Arora et al. (2013) to linear order in the perturbation – an approach that can in principle be extended to
higher orders (Ruelle, 1998; Lucarini, 2009). By demonstrating how to successfully recover generalized sensitivities, this study
paves the way for their future application in studying the dynamics of the combined carbon-climate system in different Earth
System Models. Applying our RFI method, we showed for the MPI-ESM that one can obtain these sensitivities from standard
645 C⁴MIP 1% simulations. In addition, the estimates for the linear regime obtained by employing the recovered sensitivities to
predict additional experiments give a hint into the range of perturbation strengths for which this generalized framework might
be valid as well for other models, for which data from additional experiments necessary to determine this linear regime are not
available. Since the process descriptions of the land carbon cycle are quite similar in different models, it may be assumed that
the linear range estimates obtained for MPI-ESM in the present study apply also to other models. Considering the radiative
650 land carbon response, thereby also for other models their χ_γ should fully characterize the response to temperature up to at least
6K. As a consequence, in models with temperature response similar or weaker than the MPI-ESM, χ_γ can as for the MPI-
ESM be recovered taking the full time series from the 1% experiment. Analogously, considering the generalized sensitivity
 χ_β , the experience presented in the present study for the MPI-ESM suggests that also for other models the response to CO₂



655 perturbations is linear up to 100 ppm. As a consequence, χ_β can be recovered taking data from the 1% experiment for the
first 30 years. Alternatively, as discussed in section 4, the time range for the recovery of χ_β can be extended if one takes
as forcing NPP instead of CO₂ (third approach investigated in section 4). For models with NPP response similar or weaker
than the MPI-ESM, by this approach χ_β can be recovered taking the full time series from the 1% experiment. Still, as the
relatively successful predictions in Fig. 8(b) suggest, even if χ_β is recovered by taking CO₂ as forcing for only 30 years of the
1% experiment (first approach investigated in section 4), it may still contain sufficient information to predict responses of the
660 model for a time range of 140 years.

But in addition to the carbon-cycle sensitivities considered here, our RFI method may be applied to investigate different
aspects of climate and the carbon cycle. Ragone et al. (2016) have shown how the linear response framework generalizes
the concept of equilibrium climate sensitivity (ECS) and transient climate response (TCR). Originally, ECS is defined as the
response of global temperature to an instantaneous doubling of atmospheric CO₂ from its pre-industrial value, while TCR is
665 the temperature response to a doubling of CO₂ after a 1% per year increase. Within the generalized framework, the ECS and
TCR are shown to be only particular values encoded in a linear response function.

Linear response functions can also be useful in studying “committed changes” (Wigley, 2005; Plattner et al., 2008; Jones
et al., 2009; Mauritsen and Pincus, 2017). As shown by Ragone et al. (2016), the concept of climate inertia (closely related
to committed changes) can be explicitly described within the linear response framework. Since the linear response function
670 describes the delayed response of the system to a perturbation, by deriving this function one has at hand also the information
of how the system reacts once the perturbation – for instance CO₂ emissions – ceases.

Further, linear response functions can help understanding the concept of “emergent constraints” (Nijssen and Dijkstra, 2018).
Recent studies have shown how to obtain from response functions derived from conceptual models emergent constraints for
the real Earth System (Cox et al., 2018; Williamson et al., 2019). With the method developed here, in principle such type of
675 analyses may be carried out employing instead response functions derived from Earth System Models.

As a result of accounting for the memory of the system, the linear response function gives information on the strength of
the response at all internal time scales covered by the time series underlying its recovery and probably even slightly longer
(see Fig. 8(b)). Using our method, in principle one can even compare the spectra of time scales from models to those from
observations (e.g., Forney and Rothman, 2012b). The method presented here may also be applied to analyze changes in age and
680 transit time distributions of carbon in different models, since these distributions can be derived directly from linear response
functions (Thompson and Randerson, 1999).

In all of the mentioned examples, the generality of the RFI method allows for the derivation of the appropriate linear
response functions for any model by taking only data from an arbitrary perturbation experiment and a control experiment.
Such generality opens the possibility of combining the linear response framework, which has been gaining increasing attention
685 due its wide applicability in climate science (e.g., Lucarini, 2009; Lucarini and Sarno, 2011; Lucarini et al., 2014; Ragone
et al., 2016; Lucarini et al., 2017; Aengenheyster et al., 2018; Ghil and Lucarini, 2020; Lembo et al., 2020; Bódai et al., 2020),
with model intercomparison studies, hopefully leading to a deeper understanding of critical differences encountered across
models.



Appendix A: The Max Planck Institute for Meteorology Earth System Model

690 In this appendix we give a brief description of the model employed in this study: the Max Planck Institute for Meteorology
Earth System Model (MPI-ESM; for more details see Giorgetta et al., 2013). The MPI-ESM consists of the coupled general
circulation models ECHAM6 (Stevens et al., 2013) for atmosphere, at T63/1.9° horizontal resolution with 47 vertical levels,
and MPIOM (Jungclaus et al., 2013) for ocean, with a nominal resolution of 1.5° with 40 vertical levels. In addition, the MPI-
ESM includes the subsystems JSBACH (Reick et al., 2013; Schneck et al., 2013), a land and vegetation model, and the marine
695 biogeochemistry model HAMOCC (Ilyina et al., 2013). JSBACH and HAMOCC describe respectively the land and ocean
carbon cycle in the MPI-ESM. Thus, of particular interest for our study is the subsystem JSBACH. JSBACH simulates fluxes
of energy, water, momentum and CO₂ between the land surface and atmosphere. To represent subgrid scale heterogeneity, each
grid cell of the land surface is divided into tiles, being each tile associated with a vegetation type (or “plant functional type”).
The photosynthesis scheme follows Farquhar et al. (1980) and Collatz et al. (1992). The land carbon structure is divided into
700 three vegetation pools (living tissues, carbohydrate and starch storage, and wood), four aboveground and belowground pools
for litter from woody and non-woody parts and a pool for soil carbon (humus). In addition, JSBACH includes a dynamic
vegetation scheme that allows for simulating changes in vegetation cover driven by climate.

Appendix B: Generalization of climate-carbon cycle sensitivities

In this appendix we show that indeed linear response functions generalize Friedlingstein α - β - γ sensitivities. We explain this
705 by taking the β -sensitivity of land carbon uptake as an example. The calculation of β is based on an experiment where the
CO₂-rise acts only biogeochemically, i.e. concerning the land carbon via the photosynthesis of plants. Calling $\Delta C^{bgc}(t)$ the
difference in land carbon between the perturbed and the control simulation, β is defined as

$$\beta(t) = \frac{\Delta C^{bgc}(t)}{\Delta c(t)}, \quad \Delta c(t) = c_{PI}(1.01^t - 1), \quad (\text{B1})$$

where t is the time in years elapsed since the perturbation was switched on, and $\Delta c(t)$ is the change in CO₂ concentration
710 when increasing atmospheric CO₂ each year by 1% starting from its pre-industrial value c_{PI} of the control simulation. In the
framework of linear response, one can understand $\Delta c(t)$ as perturbation and $\Delta C^{bgc}(t)$ as response so that the response formula
reads

$$\Delta C^{bgc}(t) = \int_0^t \chi_\beta(t-s) \Delta c(s) ds. \quad (\text{B2})$$

This equation defines $\chi_\beta(t)$ as the linear response function describing the biogeochemical response of land carbon to any type
715 of CO₂ perturbation $\Delta c(t)$, as long as the perturbation is sufficiently weak. Employing in particular the percent perturbation
from Eq. (B1), $\beta(t)$ is thus obtained from the linear response function $\chi_\beta(t)$ as

$$\beta(t) = \frac{1}{\Delta c(t)} \int_0^t \chi_\beta(t-s) \Delta c(s) ds. \quad (\text{B3})$$



In this way, $\chi_\beta(t)$ can be understood as a generalization of $\beta(t)$, that gives not only the response to percent-type perturbations, but also to other perturbations. Accordingly, $\chi_\beta(t)$ characterizes system properties independent of the type of perturbation, in contrast to $\beta(t)$.

Appendix C: Monotonicity of $\chi_\beta(t)$

In this appendix it is shown that the response function $\chi_\beta(t)$ is monotonic, as claimed in subsection 2.1. The argument here is actually more general, namely that the response function to changes in the input of the system (for land carbon, the Net Primary Production) is monotonic. Since $\chi_\beta(t)$ is related to $\chi_{NPP}(t)$ by Eq. (18), the monotonicity property transfers to $\chi_\beta(t)$.

Let the linear response of land carbon be described by Eq. (14):

$$\Delta C^{bgc}(t) = \int_0^t \chi_{NPP}(t-s) \Delta NPP(s) ds, \quad (C1)$$

where for simplicity we assume that $\eta(t)$ is small so that it can be neglected. If NPP is a Dirac delta function $\Delta NPP(t) = \delta(t)$, then the response is given by $\Delta C^{bgc}(t) = \chi_{NPP}(t)$. Therefore we can interpret the response function $\chi_{NPP}(t)$ as follows: If a certain number of carbon atoms enter the biosphere at time $t = 0$, the response function $\chi_{NPP}(t)$ gives the fraction of these atoms still left in the biosphere at time t .

Let $p(t)dt$ be the probability that an atom that entered the system at time $t = 0$ will leave it at time t . Then

$$P(t) := \int_0^t p(s) ds \quad (C2)$$

is the probability that an atom that entered the system at time $t = 0$ will leave the system *until* time t . Hence from the interpretation of $\chi_{NPP}(t)$ above

$$P(t) = 1 - \chi_{NPP}(t). \quad (C3)$$

From Eqs. (C2) and (C3) it follows that

$$p(t) = -\frac{d}{dt} \chi_{NPP}(t). \quad (C4)$$

But since the probability density function $p(t) \geq 0 \forall t$, then $\frac{d}{dt} \chi_{NPP}(t) \leq 0 \forall t$, i.e. $\chi_{NPP}(t)$ decays monotonically towards zero. Therefore, because $\chi_\beta(t)$ is simply a scaling of $\chi_{NPP}(t)$ given by Eq. (18), $\chi_\beta(t)$ also decays monotonically towards zero.

Appendix D: Derivation of spectrum and $\chi(t)$ when the response contains time scales much longer or much shorter than the time scales covered by data

Time scales much longer or much shorter than the time scales covered by data cannot be correctly recovered in the spectrum. Nevertheless, in this appendix we show that the wrong recovery of these extreme time scales does not strongly affect the



745 recovery of $\chi(t)$. These considerations add to the footnote remark in section 5 where we claim that such extreme time scales can be safely ignored.

First, we consider the case where the response has time scales much longer than those covered by data. Let χ at time T be given by

$$\chi(T) = \int_{-\infty}^{\infty} q(\tau) e^{-T/\tau} d\log_{10} \tau. \quad (\text{D1})$$

750 Let T be the time series length and assume that $q(\tau)$ has significant contributions at time scales $\tau \geq \tau_L$ with $\tau_L \gg T$. Then (D1) can be written as

$$\chi(T) \approx \int_{-\infty}^{\log_{10} \tau_L} q(\tau) e^{-T/\tau} d\log_{10} \tau + \int_{\log_{10} \tau_L}^{\infty} q(\tau) d\log_{10} \tau, \quad (\text{D2})$$

where $e^{-T/\tau} \approx 1$ was used in the second integral because $\tau_L \gg T$. Thereby the second term in the right-hand side of (D2) is just a constant offset

$$755 \int_{\log_{10} \tau_L}^{\infty} q(\tau) d\log_{10} \tau = k, \quad k \text{ constant.} \quad (\text{D3})$$

Hence, for internal time scales much longer than the time series length T , the correct recovery of the individual $q(\tau)$ values is not relevant for the derivation of $\chi(t)$, as long as those values combine to the correct offset in Eq. (D3). Note that because this argument is based on the condition $\tau_L \gg T$, it applies not only to $\chi(T)$ but also to all $\chi(t)$, $t < T$.

Now, we consider the case where the response has time scales much smaller than those covered by data. Let $t =: i\Delta t$, where
 760 Δt is the time step and $i \in \mathbb{N}$. If $q(\tau)$ has significant contributions at time scales $\tau \leq \tau_S$ with $\tau_S \ll \Delta t$, then for $i > 0$ Eq. (3) can be written as

$$\chi(i\Delta t) \approx \int_{\log_{10} \tau_S}^{\infty} q(\tau) e^{-i\Delta t/\tau} d\log_{10} \tau, \quad (\text{D4})$$

where $e^{-i\Delta t/\tau} \approx 0$ was used for $\tau < \tau_S$ because $\tau_S \ll \Delta t$. As a result, values of $q(\tau)$ are irrelevant to $\chi(t)$ for almost every i . The only exception is $i = 0$, where one has

$$765 \chi(0) = \int_{-\infty}^{\infty} q(\tau) d\log_{10} \tau. \quad (\text{D5})$$

Hence, for time scales much shorter than the time step Δt , the correct recovery of the individual $q(\tau)$ values is not relevant for the derivation of $\chi(t)$ as long as those values combine with the other recovered values of $q(\tau)$ to the correct $\chi(0)$ in Eq. (D5). As shown by Eq. (D4), if they combine to the wrong value, only the recovery of $\chi(0)$ is affected.

Therefore, in principle $\chi(t)$ can be correctly recovered also when the response contains much longer and much shorter
 770 time scales than those covered by data, as long as the recovered $q(\tau)$ values at these extreme time scales combine to the



correct values of the offset in Eq. (D3) and $\chi(0)$ in Eq. (D5). In Fig. D1 we show an example of recovery of the spectrum and response function in such a case. For the recovery we took data with $SNR = 6 \times 10^4$ from the 1% experiment with our toy model (see Part I). As seen, the spectrum can only be partially recovered (subfigure (a)). The recovery wrongly estimates spectral contributions at time scales longer and shorter than those covered by data, i.e. time scales larger than the time series length $T = 140$ and smaller than the time step $\Delta t = 1$. In addition, the existence of such spectral contributions at time scales not covered by data seems to also deteriorate the recovery of the spectrum at the time scales actually covered by data: In the region $1 < \tau < 140$, despite the high SNR the recovered spectrum matches the true spectrum only partially. This is probably a compensation effect where wrong information shows up in the recovered spectrum to compensate missing information on the response function. For instance, to obtain the correct $\chi(0)$, only Eq. (D5) is needed but not the correct recovery of all time scales. The same goes for obtaining the correct offset: Only Eq. (D3) is needed but not the correct recovery of all time scales from τ_L onwards.

Subfigure (b) shows the quality of the recovery of the response function $\chi(t)$. The recovered $q(\tau)$ values at long time scales, although individually wrong, combine to the correct offset in (D3): The “height” of the recovered response function almost perfectly matches that of the true response function (compare e.g. the value at $t = 140$ for the true and recovered response function). On the other hand, $\chi(0)$ is not perfectly recovered (compare the difference at $t = 0$ between the true and recovered response functions), meaning that the sum in Eq. (D5) is incorrect. Nevertheless, the recovered value is still reasonably close to the true value. Except for this small error at $\chi(0)$, the overall recovery of the response function is almost perfect.

Therefore, as claimed in section 5, this numerical example shows that even though very long and very short time scales cannot be correctly recovered in the spectrum, they do not strongly influence the recovery of $\chi(t)$. This is because they only influence the offset in Eq. (D3) and $\chi(0)$ in Eq. (D5), and those two values seem to be reasonably well recovered numerically.

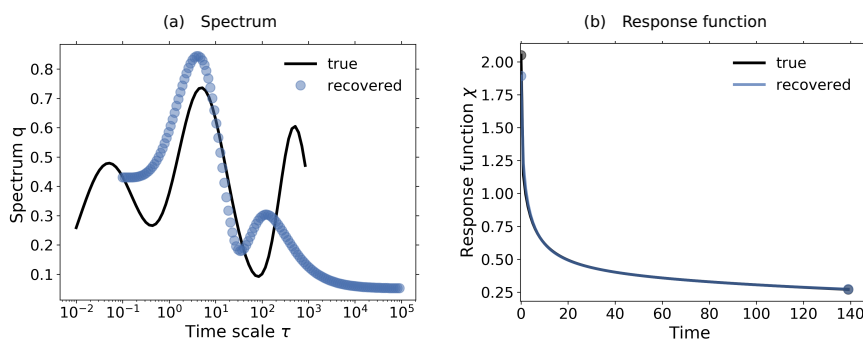


Figure D1. Recovery of spectrum and $\chi(t)$ taking a true spectrum with contributions at time scales much longer and much shorter than the time scales covered by data. For the recovery, data with $SNR = 6 \times 10^4$ from the 1% experiment with the toy model (see Part I) was taken (times series length $T = 140$ and time step $\Delta t = 1$). RFI parameters are taken as in Part I except for $M = 140$. The recovered spectrum matches only partially the true spectrum. Nevertheless, the response function $\chi(t)$ is almost perfectly recovered.



Appendix E: Recovering a discrete spectrum $q(\tau)$

This appendix gives numerical evidence for the claim in section 6 that although the RFI method assumes that the response has a continuous spectrum of many time scales, for sufficiently good signal-to-noise ratio the recovered continuous spectrum may also give a reasonable approximation to an underlying discrete spectrum of only few time scales.

795 Before we give numerical examples, one must first understand the limitations of the recovery of the spectrum. As explained in Part I, the spectrum $q(\tau)$ can only be completely recovered (for sufficiently high SNR) if it is dominated by the first components of expansion (4). By Hansen's observation (Hansen, 1989, 1990, see Part I), this means that the spectrum must be dominated by low frequencies, i.e. it must be to some extent smooth. However, an underlying discrete spectrum implies a spectrum that is instead given by "spikes" in the time scale domain. Such "spikes" can only be described by high-frequency components of
800 Eq. (4). Therefore, a discrete spectrum can be only partially recovered. To obtain a sufficiently good recovery, the solution (4) must contain many components. Hence, the data must have a sufficiently high signal-to-noise ratio. The explanation for this conclusion is the following: If many components in Eq. (4) must be recovered, the regularization parameter must be small; but a small regularization parameter requires a small noise level (see Theorem 3.3.1 in Groetsch, 1984).

With this in mind, we show in Figs. E1–E9 that at least smooth approximations to an underlying discrete spectrum can be
805 obtained. For the results we took data with $SNR \sim \mathcal{O}(10^4) - \mathcal{O}(10^5)$ from different experiments performed with the toy model described in Part I. Since the aim is to recover discrete spectra, a larger number of time scales M gives a better resolution. Therefore, we take $M = 140$. All other RFI parameters are taken according to Part I. Also, monotonicity needed not to be taken into account (step 6 of Fig. 1 in Part I).

Figures E1–E6 show results for taking data from a 1% experiment and Figs. E7–E9 from a $2 \times f_0$ experiment. We start
810 with one time scale $\tau = 37$ (Fig. E1). As expected, the spike cannot be perfectly recovered, but the recovery gives a smooth approximation to it, with peak coinciding approximately with the "true" value. On the other hand, the response function is almost perfectly recovered. This is a result of the ill-posedness of Eq. (3): In the same way that high frequencies of the spectrum are suppressed in the data by Eq. (1), they are also suppressed in the response function by Eq. (3) (see Groetsch, 1984, section 1.1). Therefore, both the true spectrum and its smooth recovery result in practically the same response function.

815 In Fig. E2, the true spectrum has two time scales, this time at $\tau = 7$ and $\tau = 100$. Similarly to Fig. E1, the time scales are recovered by a smooth approximation with peaks approximately at the true values. Also similarly to Fig. E1, the response function is almost perfectly recovered. A similar result is obtained if we take time scales that are a bit closer together, as seen in Fig. E3 ($\tau = 7$ and $\tau = 37$). Nevertheless, now the peak for the longer time scale is a worse approximation, and there is a slightly pronounced negative peak that does not reflect the true spectrum.

820 In Fig. E4, we take instead time scales $\tau = 37$ and $\tau = 100$. Here, the resolution is not sufficiently high for a recovery of each time scale separately. Instead, the recovered spectrum shows only one mode that spans both spikes. Once more the response function can be almost perfectly recovered. Taking the three time scales $\tau = 7$, $\tau = 37$ and $\tau = 100$ (Fig. E5), the smooth recovery shows only two modes: One at $\tau = 7$ with peak almost coinciding with the true value, and another with peak



in between $\tau = 37$ and $\tau = 100$. If one in addition considers a fourth time scale $\tau = 1$ (Fig. E6), once more the recovery shows
 825 only two modes. But now the mode at shorter time scales displays a longer tail that spans both $\tau = 7$ and $\tau = 1$.

The situation changes when we take for the recovery the $2\times\text{CO}_2$ experiment. According to the Laplace transform analysis
 in section 3, data from this experiment should give more information on small time scales. Figure E7 shows that this is indeed
 the case: In contrast to the recovery from Fig. E6, now the time scale $\tau = 1$ is also recovered. On the other hand, now there are
 two small negative peaks that do not reflect information from the true spectrum. Also, the resolution is not sufficiently good to
 830 recover separately the two peaks at long time scales. However, if the longest time scale is increased from $\tau = 100$ to $\tau = 228$
 (Fig. E8), a small peak can be seen around this time scale. In addition, now the peak at $\tau = 37$ matches slightly better the
 true value. In Fig. E9 we add another time scale, now at $\tau = 518$. We see that although this time scale cannot be recovered
 separately from $\tau = 228$, the peak at long time scales is more pronounced. This is in contrast to the fact that the time series
 used for the recovery reaches only $t = 140$, indicating that the method can recover information on time scales even longer than
 835 the time series length. This is in agreement with the conclusions from section 4, where in one case $\chi_\beta(t)$ was recovered from
 a time series with only 30 years but could recover responses for $t = 140$ years (see Fig. 8(b)).

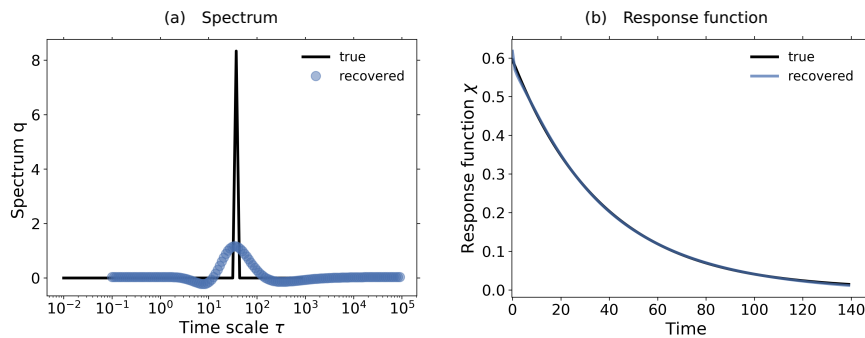


Figure E1. Spectrum q_λ and response function $\chi(t)$ recovered from a 1% experiment performed with the toy model described in Part I
 taking an underlying discrete spectrum with one time scale $\tau = 37$. The data were taken with $SNR \sim \mathcal{O}(10^4) - \mathcal{O}(10^5)$.

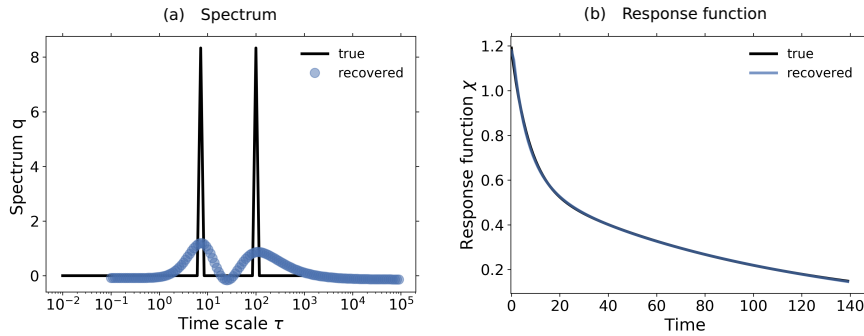


Figure E2. Spectrum q_λ and response function $\chi(t)$ recovered from a 1% experiment performed with the toy model described in Part I taking an underlying discrete spectrum with two time scales $\tau = 7, \tau = 100$. The data were taken with $SNR \sim \mathcal{O}(10^4) - \mathcal{O}(10^5)$.

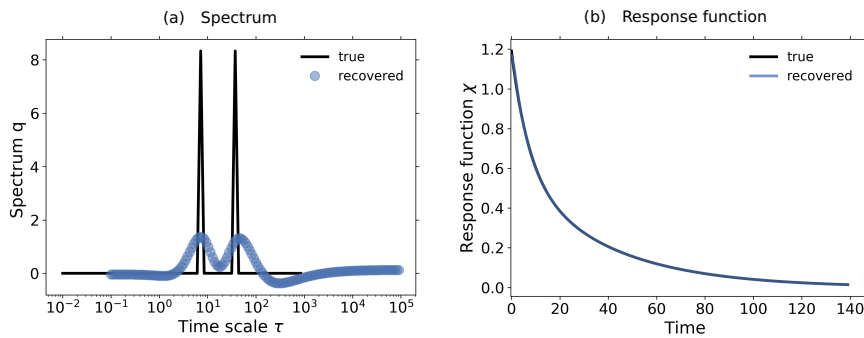


Figure E3. Spectrum q_λ and response function $\chi(t)$ recovered from a 1% experiment performed with the toy model described in Part I taking an underlying discrete spectrum with two time scales $\tau = 7, \tau = 37$. The data were taken with $SNR \sim \mathcal{O}(10^4) - \mathcal{O}(10^5)$.

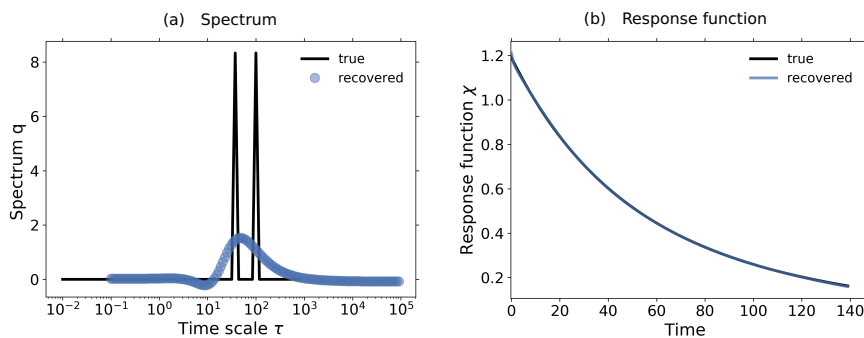


Figure E4. Spectrum q_λ and response function $\chi(t)$ recovered from a 1% experiment performed with the toy model described in Part I taking an underlying discrete spectrum with two time scales $\tau = 37, \tau = 100$. The data were taken with $SNR \sim \mathcal{O}(10^4) - \mathcal{O}(10^5)$.

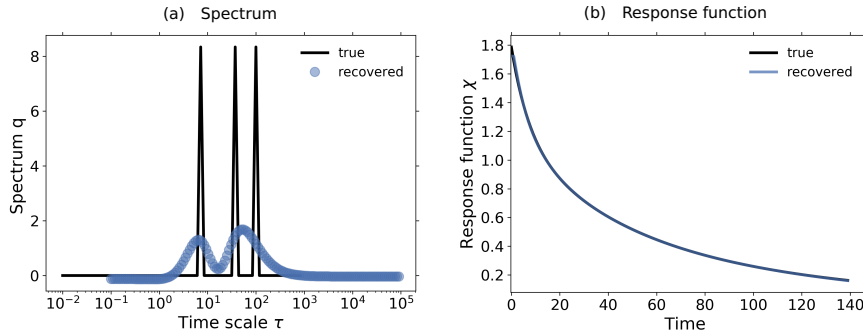


Figure E5. Spectrum q_λ and response function $\chi(t)$ recovered from a 1% experiment performed with the toy model described in Part I taking an underlying discrete spectrum with three time scales $\tau = 7, \tau = 37, \tau = 100$. The data were taken with $SNR \sim \mathcal{O}(10^4) - \mathcal{O}(10^5)$.

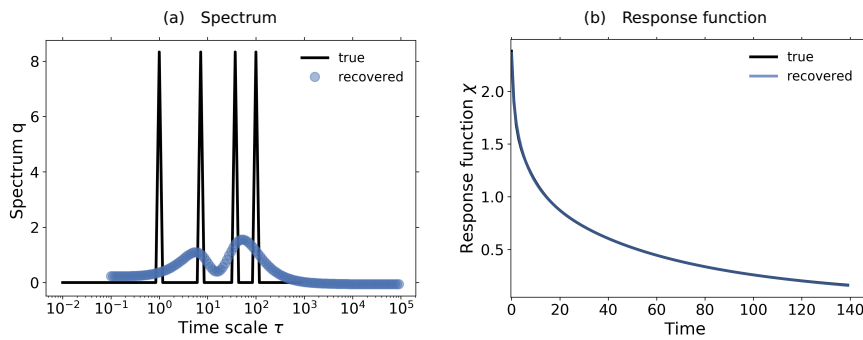


Figure E6. Spectrum q_λ and response function $\chi(t)$ recovered from a 1% experiment performed with the toy model described in Part I taking an underlying discrete spectrum with four time scales $\tau = 1, \tau = 7, \tau = 37, \tau = 100$. The data were taken with $SNR \sim \mathcal{O}(10^4) - \mathcal{O}(10^5)$.

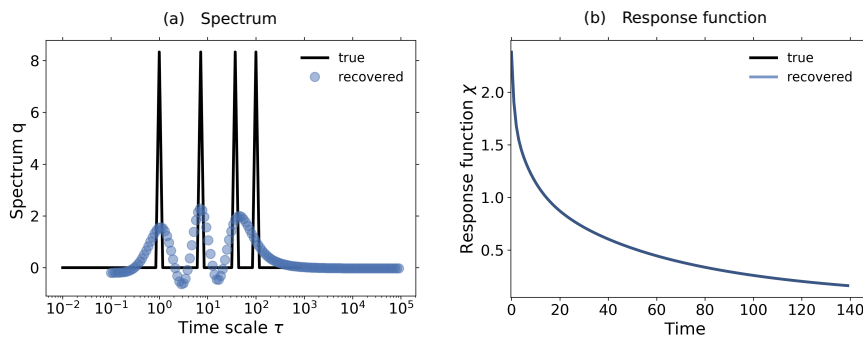


Figure E7. Spectrum q_λ and response function $\chi(t)$ recovered from a $2 \times f_0$ experiment performed with the toy model described in Part I taking an underlying discrete spectrum with four time scales $\tau = 1, \tau = 7, \tau = 37, \tau = 100$. The data were taken with $SNR \sim \mathcal{O}(10^4) - \mathcal{O}(10^5)$.

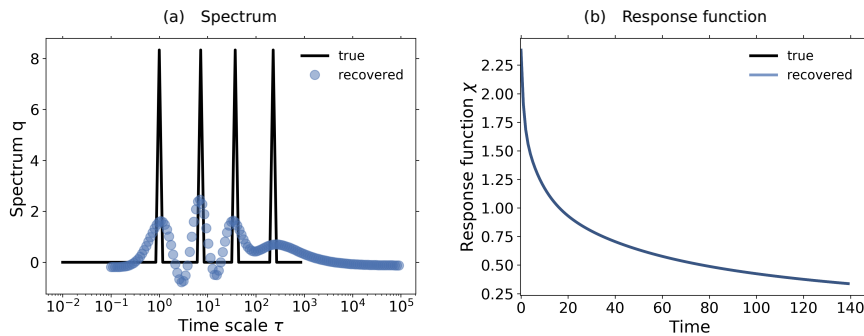


Figure E8. Spectrum q_λ and response function $\chi(t)$ recovered from a $2 \times f_0$ experiment performed with the toy model described in Part I taking an underlying discrete spectrum with four time scales $\tau = 1, \tau = 7, \tau = 37, \tau = 228$. The data were taken with $SNR \sim \mathcal{O}(10^4) - \mathcal{O}(10^5)$.

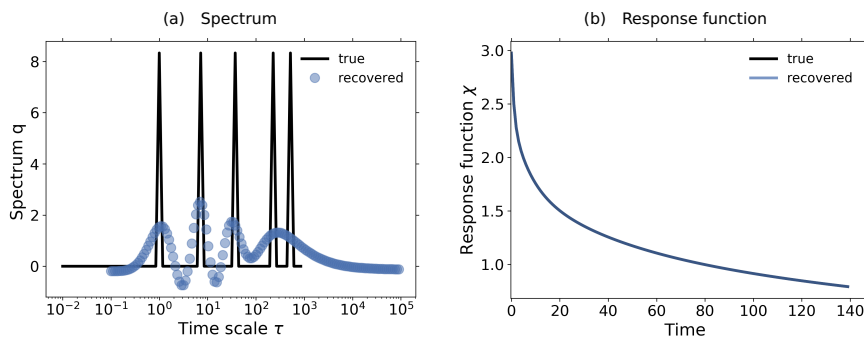


Figure E9. Spectrum q_λ and response function $\chi(t)$ recovered from a $2 \times f_0$ experiment performed with the toy model described in Part I taking an underlying discrete spectrum with five time scales $\tau = 1, \tau = 7, \tau = 37, \tau = 228, \tau = 518$. The data were taken with $SNR \sim \mathcal{O}(10^4) - \mathcal{O}(10^5)$.



Code and data availability. The scripts employed to produce the results in this paper as well as information on how to obtain the underlying data can be found at <http://hdl.handle.net/21.11116/0000-0008-0F06-2> (Torres Mendonca et al., 2021).

Author contributions. The ideas for this study were jointly developed by all authors. GTM conducted the study and wrote the first draft. All
840 authors contributed to the final manuscript.

Competing interests. The authors declare that they have no conflict of interest.

Acknowledgements. We would like to thank Andreas Chlond for his very helpful suggestions on the manuscript.



References

- Adloff, M., Reick, C. H., and Claussen, M.: Earth system model simulations show different feedback strengths of the terrestrial carbon cycle
845 under glacial and interglacial conditions, *Earth System Dynamics*, 9, 413–425, 2018.
- Aengenheyster, M., Feng, Q. Y., Van Der Ploeg, F., and Dijkstra, H. A.: The point of no return for climate action: effects of climate uncertainty
and risk tolerance., *Earth System Dynamics*, 9, 2018.
- Alexandrov, G., Oikawa, T., and Yamagata, Y.: Climate dependence of the CO₂ fertilization effect on terrestrial net primary production,
Tellus B: Chemical and Physical Meteorology, 55, 669–675, 2003.
- 850 Arora, V. K., Boer, G. J., Friedlingstein, P., Eby, M., Jones, C. D., Christian, J. R., Bonan, G., Bopp, L., Brovkin, V., Cadule, P., et al.:
Carbon–concentration and carbon–climate feedbacks in CMIP5 Earth system models, *Journal of Climate*, 26, 5289–5314, 2013.
- Arora, V. K., Katavouta, A., Williams, R. G., Jones, C. D., Brovkin, V., Friedlingstein, P., Schwinger, J., Bopp, L., Boucher, O., Cadule, P.,
et al.: Carbon-concentration and carbon-climate feedbacks in CMIP6 models, and their comparison to CMIP5 models, *Biogeosciences*
Discussions, pp. 1–124, 2019.
- 855 Bertero, M.: Linear Inverse and Ill-Posed Problems, vol. 75 of *Advances in Electronics and Electron Physics*, pp. 1–120, Academic Press,
New York, NY, [https://doi.org/https://doi.org/10.1016/S0065-2539\(08\)60946-4](https://doi.org/https://doi.org/10.1016/S0065-2539(08)60946-4), 1989.
- Bertero, M., Boccacci, P., and Maggio, F.: Regularization methods in image restoration: an application to HST images, *International Journal*
of Imaging Systems and Technology, 6, 376–386, 1995.
- Bódai, T., Lucarini, V., and Lunkeit, F.: Can we use linear response theory to assess geoengineering strategies?, *Chaos: An Interdisciplinary*
860 *Journal of Nonlinear Science*, 30, 023 124, 2020.
- Ciais, P., Sabine, C., Bala, G., Bopp, L., Brovkin, V., Canadell, J., Chhabra, A., DeFries, R., Galloway, J., Heimann, M., Jones, C., Le Quéré,
C., Myneni, R., Piao, S., and Thornton, P.: Carbon and Other Biogeochemical Cycles, in: *Climate Change 2013: The Physical Science*
Basis. Contribution of Working Group I to the Fifth Assessment Report of the Intergovernmental Panel on Climate Change, edited by
Stocker, T., Qin, D., Plattner, G.-K., Tignor, M., Allen, S., Boschung, J., Nauels, A., Xia, Y., Bex, V., and Midgley, P., pp. 465–570,
865 Cambridge University Press, Cambridge, United Kingdom and New York, NY, USA, 2013.
- Colbourn, G., Ridgwell, A., and Lenton, T.: The time scale of the silicate weathering negative feedback on atmospheric CO₂, *Global Bio-*
geochemical Cycles, 29, 583–596, 2015.
- Collatz, G. J., Ribas-Carbo, M., and Berry, J.: Coupled photosynthesis-stomatal conductance model for leaves of C₄ plants, *Functional Plant*
Biology, 19, 519–538, 1992.
- 870 Cox, P. M., Huntingford, C., and Williamson, M. S.: Emergent constraint on equilibrium climate sensitivity from global temperature vari-
ability, *Nature*, 553, 319–322, 2018.
- Engl, H. W., Hanke, M., and Neubauer, A.: Regularization of inverse problems, vol. 375, Springer Science & Business Media, 1996.
- Enting, I.: Ambiguities in the calibration of carbon cycle models, *Inverse Problems*, 6, L39, 1990.
- Enting, I. and Clisby, N.: Estimates of climatic influence on the carbon cycle, *Earth System Dynamics Discussions*, 2019, 1–21,
875 <https://doi.org/10.5194/esd-2019-41>, 2019.
- Enting, I. and Mansbridge, J.: Inversion relations for the deconvolution of CO₂ data from ice cores, *Inverse Problems*, 3, L63, 1987.
- Farquhar, G. D., von Caemmerer, S. v., and Berry, J. A.: A biochemical model of photosynthetic CO₂ assimilation in leaves of C₃ species,
Planta, 149, 78–90, 1980.
- Forney, D. and Rothman, D.: Inverse method for estimating respiration rates from decay time series, *Biogeosciences*, 9, 3601–3612, 2012a.



- 880 Forney, D. C. and Rothman, D. H.: Common structure in the heterogeneity of plant-matter decay, *Journal of the Royal Society Interface*, 9, 2255–2267, 2012b.
- Friedlingstein, P., Dufresne, J.-L., Cox, P., and Rayner, P.: How positive is the feedback between climate change and the carbon cycle?, *Tellus B*, 55, 692–700, 2003.
- Friedlingstein, P., Cox, P., Betts, R., Bopp, L., von Bloh, W., Brovkin, V., Cadule, P., Doney, S., Eby, M., Fung, I., et al.: Climate–carbon
885 cycle feedback analysis: results from the C4MIP model intercomparison, *Journal of climate*, 19, 3337–3353, 2006.
- Friedlingstein, P., O’Sullivan, M., Jones, M. W., Andrew, R. M., Hauck, J., Olsen, A., Peters, G. P., Peters, W., Pongratz, J., Sitch, S., et al.: Global carbon budget 2020, *Earth System Science Data*, 12, 3269–3340, 2020.
- Fung, I., Rayner, P., Friedlingstein, P., and Sahagian, D.: Full-form Earth System models: coupled carbon-climate interaction experiment (the ‘Flying Leap’), *IGBP Global Change Newsletter*, 2000.
- 890 Ghil, M. and Lucarini, V.: The physics of climate variability and climate change, *Reviews of Modern Physics*, 92, 035 002, 2020.
- Giorgetta, M. A., Jungclaus, J., Reick, C. H., Legutke, S., Bader, J., Böttinger, M., Brovkin, V., Crueger, T., Esch, M., Fieg, K., et al.: Climate and carbon cycle changes from 1850 to 2100 in MPI-ESM simulations for the Coupled Model Intercomparison Project phase 5, *Journal of Advances in Modeling Earth Systems*, 5, 572–597, 2013.
- Gregory, J. M., Ingram, W., Palmer, M., Jones, G., Stott, P., Thorpe, R., Lowe, J., Johns, T., and Williams, K.: A new method for diagnosing
895 radiative forcing and climate sensitivity, *Geophysical research letters*, 31, 2004.
- Gregory, J. M., Jones, C., Cadule, P., and Friedlingstein, P.: Quantifying carbon cycle feedbacks, *Journal of Climate*, 22, 5232–5250, 2009.
- Groetsch, C.: The theory of Tikhonov regularization for Fredholm equations, Boston Pitman Publication, Boston, MA, 1984.
- Hansen, P. C.: Regularization, GSVD and truncated GSVD, *BIT numerical mathematics*, 29, 491–504, 1989.
- Hansen, P. C.: The discrete Picard condition for discrete ill-posed problems, *BIT Numerical Mathematics*, 30, 658–672, 1990.
- 900 Hansen, P. C.: Deconvolution and regularization with Toeplitz matrices, *Numerical Algorithms*, 29, 323–378, 2002.
- Hansen, P. C.: Discrete inverse problems: insight and algorithms, vol. 7, Siam, 2010.
- Ilyina, T. and Friedlingstein, P.: Biogeochemical cycles and climate change, White paper on WCRP Grand Challenge (World Climate Research Programme), 2016.
- Ilyina, T., Six, K. D., Segschneider, J., Maier-Reimer, E., Li, H., and Núñez-Riboni, I.: Global ocean biogeochemistry model HAMOCC:
905 Model architecture and performance as component of the MPI-Earth system model in different CMIP5 experimental realizations, *Journal of Advances in Modeling Earth Systems*, 5, 287–315, 2013.
- Istratov, A. A. and Vyvenko, O. F.: Exponential analysis in physical phenomena, *Review of Scientific Instruments*, 70, 1233–1257, 1999.
- Jones, C., Lowe, J., Liddicoat, S., and Betts, R.: Committed terrestrial ecosystem changes due to climate change, *Nature Geoscience*, 2, 484–487, 2009.
- 910 Joos, F., Bruno, M., Fink, R., Siegenthaler, U., Stocker, T. F., Le Quere, C., and Sarmiento, J. L.: An efficient and accurate representation of complex oceanic and biospheric models of anthropogenic carbon uptake, *Tellus B*, 48, 397–417, 1996.
- Joos, F., Roth, R., Fuglestedt, J., Peters, G., Enting, I., Bloh, W. v., Brovkin, V., Burke, E., Eby, M., Edwards, N., et al.: Carbon dioxide and climate impulse response functions for the computation of greenhouse gas metrics: a multi-model analysis, *Atmospheric Chemistry and Physics*, 13, 2793–2825, 2013.
- 915 Jungclaus, J., Fischer, N., Haak, H., Lohmann, K., Marotzke, J., Matei, D., Mikolajewicz, U., Notz, D., and Von Storch, J.: Characteristics of the ocean simulations in the Max Planck Institute Ocean Model (MPIOM) the ocean component of the MPI-Earth system model, *Journal of Advances in Modeling Earth Systems*, 5, 422–446, 2013.



- Lanczos, C.: Applied Analysis, Mathematics series, Prentice-Hall, Upper Saddle River, NJ, 1956.
- Landl, G., Langthaler, T., Engl, H. W., and Kauffmann, H. F.: Distribution of event times in time-resolved fluorescence: the exponential
920 series approach—algorithm, regularization, analysis, *Journal of Computational Physics*, 95, 1–28, 1991.
- Lembo, V., Lucarini, V., and Ragone, F.: Beyond forcing scenarios: predicting climate change through response operators in a coupled general
circulation model, *Scientific Reports*, 10, 1–13, 2020.
- Lord, N. S., Ridgwell, A., Thorne, M., and Lunt, D.: An impulse response function for the “long tail” of excess atmospheric CO₂ in an Earth
system model, *Global Biogeochemical Cycles*, 30, 2–17, 2016.
- 925 Lucarini, V.: Evidence of dispersion relations for the nonlinear response of the Lorenz 63 system, *Journal of Statistical Physics*, 134, 381–400,
2009.
- Lucarini, V. and Sarno, S.: A statistical mechanical approach for the computation of the climatic response to general forcings, *Nonlinear
Processes in Geophysics*, 18, 7–28, 2011.
- Lucarini, V., Blender, R., Herbert, C., Ragone, F., Pascale, S., and Wouters, J.: Mathematical and physical ideas for climate science, *Reviews
930 of Geophysics*, 52, 809–859, <https://doi.org/10.1002/2013RG000446>, 2014.
- Lucarini, V., Ragone, F., and Lunkeit, F.: Predicting climate change using response theory: Global averages and spatial patterns, *Journal of
Statistical Physics*, 166, 1036–1064, 2017.
- MacMartin, D. G. and Kravitz, B.: Dynamic climate emulators for solar geoengineering, *Atmospheric Chemistry and Physics*, 16, 15789–
15799, 2016.
- 935 Maier-Reimer, E. and Hasselmann, K.: Transport and storage of CO₂ in the ocean - an inorganic ocean-circulation carbon cycle model,
Climate dynamics, 2, 63–90, 1987.
- Marotzke, J., Jakob, C., Bony, S., Dirmeyer, P. A., O’Gorman, P. A., Hawkins, E., Perkins-Kirkpatrick, S., Le Quere, C., Nowicki, S.,
Paulavets, K., et al.: Climate research must sharpen its view, *Nature climate change*, 7, 89–91, 2017.
- Mauritsen, T. and Pincus, R.: Committed warming inferred from observations, *Nature Climate Change*, 7, 652, 2017.
- 940 McWhirter, J. and Pike, E. R.: On the numerical inversion of the Laplace transform and similar Fredholm integral equations of the first kind,
Journal of Physics A: Mathematical and General, 11, 1729, 1978.
- Morozov, V. A.: On the solution of functional equations by the method of regularization, in: *Doklady Akademii Nauk*, vol. 167, pp. 510–512,
Russian Academy of Sciences, 1966.
- Nijssse, F. J. and Dijkstra, H. A.: A mathematical approach to understanding emergent constraints, *Earth System Dynamics*, 9, 999–1012,
945 2018.
- Phillips, D. L.: A technique for the numerical solution of certain integral equations of the first kind, *Journal of the ACM (JACM)*, 9, 84–97,
1962.
- Plattner, G.-K., Knutti, R., Joos, F., Stocker, T., Von Bloh, W., Brovkin, V., Cameron, D., Driesschaert, E., Dutkiewicz, S., Eby, M., et al.:
Long-term climate commitments projected with climate–carbon cycle models, *Journal of Climate*, 21, 2721–2751, 2008.
- 950 Pongratz, J., Caldeira, K., Reick, C. H., and Claussen, M.: Coupled climate–carbon simulations indicate minor global effects of wars and
epidemics on atmospheric CO₂ between ad 800 and 1850, *The Holocene*, 21, 843–851, 2011.
- Ragone, F., Lucarini, V., and Lunkeit, F.: A new framework for climate sensitivity and prediction: a modelling perspective, *Climate dynamics*,
46, 1459–1471, 2016.
- Raich, J. W. and Potter, C. S.: Global patterns of carbon dioxide emissions from soils, *Global biogeochemical cycles*, 9, 23–36, 1995.



- 955 Reick, C., Raddatz, T., Brovkin, V., and Gayler, V.: Representation of natural and anthropogenic land cover change in MPI-ESM, *Journal of Advances in Modeling Earth Systems*, 5, 459–482, 2013.
- Rubino, M., Etheridge, D., Trudinger, C., Allison, C., Rayner, P., Enting, I., Mulvaney, R., Steele, L., Langenfelds, R., Sturges, W., et al.: Low atmospheric CO₂ levels during the Little Ice Age due to cooling-induced terrestrial uptake, *Nature Geoscience*, 9, 691–694, 2016.
- Ruelle, D.: Nonequilibrium statistical mechanics near equilibrium: computing higher-order terms, *Nonlinearity*, 11, 5, 1998.
- 960 Schneck, R., Reick, C. H., and Raddatz, T.: Land contribution to natural CO₂ variability on time scales of centuries, *Journal of Advances in Modeling Earth Systems*, 5, 354–365, 2013.
- Schwinger, J., Tjiputra, J. F., Heinze, C., Bopp, L., Christian, J. R., Gehlen, M., Ilyina, T., Jones, C. D., Salas-Mélia, D., Segschneider, J., et al.: Nonlinearity of ocean carbon cycle feedbacks in CMIP5 earth system models, *Journal of Climate*, 27, 3869–3888, 2014.
- Stevens, B., Giorgetta, M., Esch, M., Mauritsen, T., Crueger, T., Rast, S., Salzmann, M., Schmidt, H., Bader, J., Block, K., et al.: Atmospheric component of the MPI-M Earth system model: ECHAM6, *Journal of Advances in Modeling Earth Systems*, 5, 146–172, 2013.
- 965 Taylor, K. E., Stouffer, R. J., and Meehl, G. A.: An overview of CMIP5 and the experiment design, *Bulletin of the American Meteorological Society*, 93, 485–498, 2012.
- Thompson, M. V. and Randerson, J. T.: Impulse response functions of terrestrial carbon cycle models: method and application, *Global Change Biology*, 5, 371–394, 1999.
- 970 Tikhonov, A. N.: Solution of incorrectly formulated problems and the regularization method, in: *Dokl. Akad. Nauk.*, vol. 151, pp. 1035–1038, 1963.
- Torres Mendonca, G., Pongratz, J., and Reick, C. H.: Supplementary material for “Identification of linear response functions from arbitrary perturbation experiments in the presence of noise - Part II. Application to the land carbon cycle in the MPI Earth System Model”, MPG Publication Repository - MPG. PuRe, <http://hdl.handle.net/21.11116/0000-0008-0F06-2>, 2021.
- 975 Wigley, T. M.: The climate change commitment, *Science*, 307, 1766–1769, 2005.
- Williamson, M. S., Cox, P. M., and Nijssen, F. J.: Theoretical foundations of emergent constraints: relationships between climate sensitivity and global temperature variability in conceptual models, *Dynamics and Statistics of the Climate System*, 3, dzy006, 2019.